

Vibrationally resolved two-photon electronic spectra including vibrational pre-excitation: Theory and application to VIPER spectroscopy with two-photon excitation

Cite as: J. Chem. Phys. **158**, 064201 (2023); <https://doi.org/10.1063/5.0132608>

Submitted: 29 October 2022 • Accepted: 11 January 2023 • Accepted Manuscript Online: 13 January 2023 • Published Online: 08 February 2023

 Maximiliane Horz,  Hafiz M. A. Masood,  Hendrik Brunst, et al.

COLLECTIONS

Paper published as part of the special topic on [Celebrating 25 Years of Two-dimensional Infrared \(2D IR\) Spectroscopy](#)



[View Online](#)



[Export Citation](#)



[CrossMark](#)

ARTICLES YOU MAY BE INTERESTED IN

[An efficient time-domain implementation of the multichromophoric Förster resonant energy transfer method](#)

The Journal of Chemical Physics **158**, 064103 (2023); <https://doi.org/10.1063/5.0136652>

[Simulation of two-dimensional infrared Raman spectroscopy with application to proteins](#)

The Journal of Chemical Physics **158**, 064106 (2023); <https://doi.org/10.1063/5.0138958>

[Machine learning matrix product state ansatz for strongly correlated systems](#)

The Journal of Chemical Physics **158**, 064108 (2023); <https://doi.org/10.1063/5.0133399>

 **The Journal of Chemical Physics** **Special Topics** Open for Submissions [Learn More](#)

Vibrationally resolved two-photon electronic spectra including vibrational pre-excitation: Theory and application to VIPER spectroscopy with two-photon excitation

Cite as: *J. Chem. Phys.* **158**, 064201 (2023); doi: [10.1063/5.0132608](https://doi.org/10.1063/5.0132608)

Submitted: 29 October 2022 • Accepted: 11 January 2023 •

Published Online: 8 February 2023










View Online



Export Citation



CrossMark

Maximiliane Horz,¹  Hafiz M. A. Masood,²  Hendrik Brunst,²  Javier Cerezo,^{3,4}  David Picconi,^{1,a)}  Hannah Vormann,¹  Madhava Shyam Niraghatam,¹  Luuk J. G. W. van Wilderen,²  Jens Bredenbeck,^{2,b)}  Fabrizio Santoro,^{4,b)}  and Irene Burghardt^{1,b)} 

AFFILIATIONS

¹Institute of Physical and Theoretical Chemistry, Goethe University Frankfurt, Max-von-Laue-Str. 7, 60438 Frankfurt, Germany

²Institute of Biophysics, Goethe University Frankfurt, Max-von-Laue-Str. 1, 60438 Frankfurt, Germany

³Departamento de Química and Institute for Advanced Research in Chemical Sciences (IAdChem), Universidad Autónoma de Madrid, 28049 Madrid, Spain

⁴Consiglio Nazionale delle Ricerche – CNR, Istituto di Chimica dei Composti Organo Metallici (ICCOM-CNR), SS di Pisa, Via G. Moruzzi 1, I-56124 Pisa, Italy

Note: This paper is part of the JCP Special Topic on Celebrating 25 Years of Two-Dimensional Infrared (2D IR) Spectroscopy.

a) Current address: Zernike Institute for Advanced Materials, Faculty of Science and Engineering, University of Groningen, Nijenborgh 4, 9747 AG, Groningen, The Netherlands.

b) Authors to whom correspondence should be addressed: bredenbeck@biophysik.uni-frankfurt.de; fabrizio.santoro@pi.iccom.cnr.it; and burghardt@chemie.uni-frankfurt.de

ABSTRACT

Following up on our previous work on vibrationally resolved electronic absorption spectra including the effect of vibrational pre-excitation [von Cosel *et al.*, *J. Chem. Phys.* **147**, 164116 (2017)], we present a combined theoretical and experimental study of two-photon-induced vibronic transitions in polyatomic molecules that are probed in the Vibrationally Promoted Electronic Resonance experiment using two-photon excitation (2P-VIPER). In order to compute vibronic spectra, we employ time-independent and time-dependent methods based on the evaluation of Franck–Condon overlap integrals and Fourier transformations of time-domain correlation functions, respectively. The time-independent approach uses a generalized version of the *FCClasses* method, while the time-dependent approach relies on the analytical evaluation of Gaussian moments within the harmonic approximation, including Duschinsky rotation effects. For the Coumarin 6 dye, two-dimensional 2P-VIPER experiments involving excitation to the lowest-lying singlet excited state (S_1) are presented and compared with corresponding one-photon VIPER spectra. In both cases, coumarin ring modes and a CO stretch mode show VIPER activity, albeit with different relative intensities. Selective pre-excitation of these modes leads to a pronounced redshift of the low-frequency edge of the electronic absorption spectrum, which is a prerequisite for the VIPER experiment. Theoretical analysis underscores the role of interference between Franck–Condon and Herzberg–Teller effects in the two-photon experiment, which is at the root of the observed intensity distribution.

Published under an exclusive license by AIP Publishing. <https://doi.org/10.1063/5.0132608>

I. INTRODUCTION

In recent years, combined electronic-vibrational nonlinear spectroscopies have gained increased attention.^{1–4} In this context,

the Vibrationally Promoted Electronic Resonance (VIPER) experiment has led to diverse applications in two-dimensional infrared (2D-IR) spectroscopy and photochemistry.^{5–7} VIPER was originally introduced by two of us⁵ in order to generate long-lived infrared (IR)

signals, permitting us to investigate chemical exchange. The two-dimensional (2D) VIPER experiment combines selective IR pump excitation with a subsequent actinic UV/Vis or near-IR (NIR) pulse and an IR probe pulse, as illustrated in Fig. 1. The actinic pulse is off-resonant and therefore, by design, not able to induce an electronic transition in the absence of vibrational pre-excitation. Hence, selective vibrational excitation via a narrow-band IR pulse or pairs of IR pulses in a Fourier transformation set-up (see Fig. 1) enables the excitation of a sub-ensemble of molecules. For example, the VIPER experiment can be employed to selectively cleave photolabile protecting groups (PPGs).⁸ In particular, selectivity has been achieved for PPGs that are chemically identical but differ in isotopic composition.⁶

In order to theoretically predict VIPER-active modes for polyatomic chromophores, we previously introduced the computation of vibrationally resolved electronic spectra including the effect of vibrational pre-excitation.⁹ In the present work, we extend this treatment to the electronic excitation via two-photon (2P) absorption^{10,11}—such that the actinic UV/Vis pulse of the VIPER experiment is replaced by a NIR pulse inducing a 2P transition—and present experimental results and a complementary theoretical analysis for the laser dye Coumarin 6. Using 2P absorption provides many advantages, such as increased spatial resolution, increased penetration depth, and minimized photodamage.¹² Especially, the latter makes 2P absorption highly attractive for biological systems and medical applications.

Our theoretical analysis proceeds in an analogous way to our previous treatment in the case of one-photon (1P) absorption by means of vibrationally resolved linear absorption spectra, including vibrational pre-excitation.⁹ However, since the electronic transitions involved are usually weakly allowed or forbidden in case of 2P absorption, we go beyond a Franck–Condon (FC) treatment and include Herzberg–Teller (HT) terms,^{13,14} which turn out to play a non-negligible role.

Coumarin 6, the system under investigation, is of practical interest since coumarin-based PPGs, in general, are widely used due to their favorable experimental properties, such as a high quantum

yield and fast photorelease rates.⁸ In the context of VIPER spectroscopy, Coumarin 6 was previously studied in a proof-of-principle investigation showing that the VIPER experiment is capable of giving access to exchange beyond the vibrational lifetime T_1 .⁵ Thus, VIPER excitation of Coumarin 6 was analyzed in our previous theoretical and computational study⁹ dealing with 1P excitation and is now chosen to illustrate the differences between 1P and 2P VIPER excitation. For this reason, the lowest-lying singlet state (S_1) is addressed, although this state of Coumarin 6 is not a highly 2P active state (see Sec. IV A and Sec. S1 of the supplementary material for an overview of the spectroscopic properties of the low-lying singlet states of Coumarin 6).

Since the VIPER experiment relies on vibronic coupling effects, theoretical analysis permits gaining a handle on the VIPER efficiency of individual molecular modes. Using a similar approach as in our previous one-photon VIPER study,⁹ we aim to predict favorable modes for VIPER excitation in the case of 2P absorption. In line with our previous study, we will not simulate the full 2D VIPER nonlinear signal obtained by the actual pump-probe sequence. Our analysis is instead focused on the linear vibronic spectra resulting from the combined IR and NIR excitation, where we apply a harmonic model including Duschinsky effects,^{14–16} i.e., mode mixing between the ground and excited states. We employ a high-dimensional representation of the vibronic Hamiltonian, parameterized in full normal-mode space, based upon ground-state and excited-state electronic structure calculations. To this end, a time-independent (TI) version of the *FCclasses* method,^{17,18} permitting the efficient evaluation of Franck–Condon overlap integrals, is employed. In the present context, the recent *FCclasses3* version^{18,19} is used, which is specifically adapted to include 1P and 2P absorption in the presence of vibrational pre-excitation. Complementary to the time-independent (TI) *FCclasses* approach, a time-dependent (TD) approach is employed, which relies on the computation of correlation functions by the analytical evaluation of Gaussian moments within a harmonic approximation that includes Duschinsky effects.⁹

The manuscript is organized as follows: Sec. II addresses the computation of two-photon VIPER spectra based on complementary time-independent (TI) and time-dependent (TD) approaches, Sec. III briefly summarizes experimental and computational procedures, Sec. IV details the results of this study, and Sec. V concludes.

II. COMPUTATION OF VIBRONIC TWO-PHOTON SPECTRA FROM A VIBRATIONALLY PRE-EXCITED STATE

In this section, formal expressions for vibronically resolved two-photon cross-sections are given within a time-independent framework (Sec. II A) and a time-dependent framework (Sec. II B). As preliminary remarks, we will first introduce some notation.

The computation of vibronic spectra typically proceeds from a thermal ensemble of vibrational states, populated according to the Boltzmann distribution.²⁰ In contrast, the present study is concerned with two-photon excitation from a non-equilibrium state where a single vibrational mode is placed into its first excited state

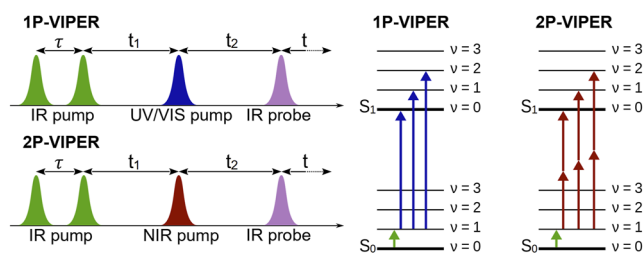


FIG. 1. Comparison of the time-domain 1P-VIPER and 2P-VIPER two-dimensional pulse sequences. The pulse sequences are initiated by a pair of IR pump pulses with a delay τ , which yields the ω_{pump} dimension in the 2D spectrum (see Fig. 3). The IR pump pulses are followed by an off-resonant UV/Vis or NIR pump pulse that leads to electronic excitation of vibrationally pre-excited species. Detection by the IR probe pulse yields the ω_{probe} dimension of the 2D spectrum (see Fig. 3). The vibronic excitation schemes pertaining to 1P-VIPER and 2P-VIPER, with UV/Vis or NIR electronic excitation, are schematically depicted on the right hand side.

by vibrational pre-excitation in the electronic ground state, by analogy with our previous study of the 1P-VIPER experiment.⁹ The present study will be restricted to a zero-temperature setting, and we will focus on the pre-excitation of high-frequency modes for which thermal excitation is negligible.

In the following, the potential energy surfaces (PESs) are taken as harmonic, and the vibrational states are defined in terms of the number of quanta in each vibrational normal mode: $|\mathbf{v}\rangle = |v_1\rangle \otimes |v_2\rangle \otimes \dots \otimes |v_{N_n}\rangle$. Vibrational states pertaining to the electronic ground state are denoted $|\mathbf{v}_g\rangle$, while vibrational states in the excited electronic state are denoted $|\mathbf{v}_e\rangle$. The vibrational ground state in the electronic ground state ($|g\rangle$) is denoted $|\mathbf{v}_g\rangle = |0_{g1}\rangle \otimes \dots \otimes |0_{gN_n}\rangle \equiv |\mathbf{0}_g\rangle$, and a vibrational state with pre-excitation of the k th mode in the electronic ground state is denoted $|\mathbf{v}_{gk}\rangle = |0_{g1}\rangle \otimes |0_{g2}\rangle \dots |1_{gk}\rangle \dots |0_{gN_n-1}\rangle \otimes |0_{gN_n}\rangle \equiv |\mathbf{0}_g + \mathbf{1}_{gk}\rangle$. Combined vibrational-electronic (i.e., vibronic) states are referred to as $|\mathbf{v}_n\rangle \otimes |n\rangle$, where the electronic space $\{|n\rangle\}$ is restricted to the electronic ground state ($|g\rangle$) and the relevant excited state ($|e\rangle$) in the following discussion.

As in Ref. 9, we are going to work in a normal-mode representation throughout, taking into account that the normal modes of the initial state $\mathbf{Q}_g = \{Q_{g1}, \dots, Q_{gN_n}\}$ and the final state $\mathbf{Q}_e = \{Q_{e1}, \dots, Q_{eN_n}\}$ are different. Neglecting the effects of rotation (which can be minimized as explained, e.g., in Ref. 17), these sets of modes are related by the Duschinsky rotation,¹⁵

$$\mathbf{Q}_e = \mathbf{J}\mathbf{Q}_g + \mathbf{K}, \quad (1)$$

where the transformation matrix \mathbf{J} and the displacement vector \mathbf{K} are defined by

$$\mathbf{J} = \mathbf{L}_e^{-1}\mathbf{L}_g \quad \text{and} \quad \mathbf{K} = \mathbf{L}_e^{-1}(\mathbf{q}_g^{\text{eq}} - \mathbf{q}_e^{\text{eq}}), \quad (2)$$

with \mathbf{L} the normal-mode matrix relating the normal modes \mathbf{Q} to mass-weighted Cartesian coordinates $\mathbf{q} = (q_1, q_2, \dots, q_{3N})$,

$$\mathbf{Q} = \mathbf{L}^{-1}(\mathbf{q} - \mathbf{q}^{\text{eq}}). \quad (3)$$

In Eq. (2), the equilibrium structures of the initial and final state are termed \mathbf{q}_g^{eq} and \mathbf{q}_e^{eq} . As a note regarding Eq. (1), we employed the inverse transformation in Ref. 9, i.e., $\mathbf{Q}_g = \mathbf{J}'\mathbf{Q}_e + \mathbf{K}'$, where $\mathbf{J}' = \mathbf{J}^T$ and $\mathbf{K}' = -(\mathbf{J})^T\mathbf{K}$.

Next, the time-independent and time-dependent approaches to the computation of two-photon absorption (2PA) cross sections will be detailed.

A. Time-independent approach

1. Vibronic 2PA cross section

The 2PA cross-section for a transition from an initial vibronic state $|\mathbf{v}_g\rangle$ —which could correspond to the vibronic ground state $|\mathbf{0}_g\rangle$ or to a vibrationally pre-excited state $|\mathbf{0}_g + \mathbf{1}_{gk}\rangle$ —to a set of excited states $|\mathbf{v}_e\rangle$ is given as^{21,22}

$$\sigma_{2\text{PA}}(\omega) = \frac{4\pi^3 a_0^5 \alpha}{15c} \omega^2 \sum_{\mathbf{v}_e} \delta_{2\text{PA}}^{(\mathbf{v}_e)} L\left(\frac{\Delta E_{ge} - E_{\mathbf{v}_g} + E_{\mathbf{v}_e}}{\hbar} - 2\omega; \Gamma\right), \quad (4)$$

where α is the fine structure constant, c is the speed of light, a_0 is the Bohr radius; furthermore, ΔE_{ge} denotes the electronic adiabatic energy gap, $E_{\mathbf{v}_g}$ is the vibrational energy pertaining to the initial vibrational state $|\mathbf{0}_g\rangle$, and $E_{\mathbf{v}_e}$ is the vibrational energy pertaining to the final vibrational state $|\mathbf{v}_e\rangle$. Finally, L is a line shape function, here taken as a Lorentzian with width Γ ,

$$L\left(\frac{E}{\hbar} - 2\omega; \Gamma\right) = \frac{1}{\pi} \frac{\Gamma}{((E/\hbar) - 2\omega)^2 + \Gamma^2}. \quad (5)$$

In the summation over final states in Eq. (4), $\delta_{2\text{PA}}^{(\mathbf{v}_e)}$ is the orientationally averaged 2PA probability,²³ which can be expressed as a sum of components,

$$\delta_{2\text{PA}}^{(\mathbf{v}_e)} = \sum_{I \in \{F, G, H\}} I \delta_I^{(\mathbf{v}_e)} = \sum_{I \in \{F, G, H\}} I S_{\eta_i \tau_i}^{(\mathbf{v}_e)} S_{\eta_i' \tau_i'}^{(\mathbf{v}_e)*}, \quad (6)$$

where $S_{\eta_i \tau_i}^{(\mathbf{v}_e)}$ is the two-photon transition matrix element, a second-rank tensor, for the transition $\mathbf{v}_g \rightarrow \mathbf{v}_e$, as further specified below. For the components $I \in \{F, G, H\}$, specific index combinations (η_i, τ_i) and (η_i', τ_i') are found to result from orientational averaging, e.g., for $I = F$, $(\eta_F = \alpha, \tau_F = \alpha)$, $(\eta_F' = \beta, \tau_F' = \beta)$, where all tensor indices relate to Cartesian components (x, y, z) . Furthermore, the r.h.s. of Eq. (6) is taken to imply that a summation is carried out over these Cartesian components, as can be seen from the following explicit expression:²¹⁻²³

$$\delta_{2\text{PA}}^{(\mathbf{v}_e)} = F \delta_F^{(\mathbf{v}_e)} + G \delta_G^{(\mathbf{v}_e)} + H \delta_H^{(\mathbf{v}_e)} \\ = \sum_{\alpha\beta} \left(F S_{\alpha\alpha}^{(\mathbf{v}_e)} S_{\beta\beta}^{(\mathbf{v}_e)*} + G S_{\alpha\beta}^{(\mathbf{v}_e)} S_{\alpha\beta}^{(\mathbf{v}_e)*} + H S_{\alpha\beta}^{(\mathbf{v}_e)} S_{\beta\alpha}^{(\mathbf{v}_e)*} \right). \quad (7)$$

The prefactors $\{F, G, H\}$ depend on the polarization vectors of the electromagnetic field, e.g., $F = G = H = 2$ for linearly polarized light and $F = -2$, $G = H = 3$ for circularly polarized light.

The two-photon transition matrix element $S_{\eta\tau}$ is generally evaluated by a sum-over-states (SOS) formula. The SOS expansion reads as follows in terms of intermediate vibronic states $|j, \mathbf{v}_j\rangle$:^{21,22,24}

$$S_{\eta\tau}^{(\mathbf{v}_e)}(\omega) = \sum_{j, \mathbf{v}_j} \left(\frac{\langle g, \mathbf{v}_g | \mu_\eta | j, \mathbf{v}_j \rangle \langle j, \mathbf{v}_j | \mu_\tau | e, \mathbf{v}_e \rangle}{\omega_{j, \mathbf{v}_j} - \omega} \right. \\ \left. + \frac{\langle g, \mathbf{v}_g | \mu_\tau | j, \mathbf{v}_j \rangle \langle j, \mathbf{v}_j | \mu_\eta | e, \mathbf{v}_e \rangle}{\omega_{j, \mathbf{v}_j} - \omega} \right), \quad (8)$$

where ω_{j, \mathbf{v}_j} denote the vibronic frequencies of the intermediate states. As mentioned above, the tensor indices (η, τ) refer to pairs of (x, y, z) components, which are here seen to relate to Cartesian components μ_η and μ_τ of the dipole operator, such that the two-photon transition matrix element $S_{\eta\tau}$ is given by products of transition dipole matrix elements involving the intermediate states, whose participation is determined by the energy difference appearing in the denominator.

Assuming that vibronic level spacings are much smaller than electronic transition frequencies, the approximation $\omega_{j, \mathbf{v}_j} \sim \omega_j$ is usually made,^{21,22} such that the vibronic transition matrix elements are obtained in the following, simplified form:

$$S_{\eta\tau}^{(\mathbf{v}_e)}(\omega) \simeq \langle \mathbf{v}_g | S_{\eta\tau}^{\text{el}} | \mathbf{v}_e \rangle, \quad (9)$$

where the SOS expression for the electronic transition matrix element $S_{\eta\tau}^{\text{el}}$ reads

$$S_{\eta\tau}^{\text{el}}(\omega) = \sum_j \left(\frac{\langle g|\mu_\eta|j\rangle\langle j|\mu_\tau|e\rangle}{\omega_j - \omega} + \frac{\langle g|\mu_\tau|j\rangle\langle j|\mu_\eta|e\rangle}{\omega_j - \omega} \right), \quad (10)$$

and the sum is reduced to intermediate electronic states $|j\rangle$. This quantity is evaluated in electronic structure programs, such as Dalton,²⁵ using a quadratic response function, and it generally depends on the nuclear geometry.

As a result, the 2PA cross-section can be written as follows:

$$\sigma_{2\text{PA}}(\omega) = \frac{4\pi^3 a_0^5 \alpha}{15c} \omega^2 \sum_{I \in \{F,G,H\}} I \sum_{\mathbf{v}_e} \langle \mathbf{v}_g | S_{\eta\tau}^{\text{el}} | \mathbf{v}_e \rangle \langle \mathbf{v}_e | S_{\eta'\tau'}^{\text{el}*} | \mathbf{v}_g \rangle \times L \left(\frac{\Delta E_{ge} - E_{\mathbf{v}_g} + E_{\mathbf{v}_e}}{\hbar} - 2\omega; \Gamma \right), \quad (11)$$

where we used that $S_{\eta\tau}^{\text{el}*} = \langle \mathbf{v}_g | S_{\eta\tau}^{\text{el}} | \mathbf{v}_e \rangle^* = \langle \mathbf{v}_e | S_{\eta\tau}^{\text{el}*} | \mathbf{v}_g \rangle$.

2. Franck-Condon and Herzberg-Teller contributions

In practice, the electronic transition matrix elements of Eq. (9) are expanded to linear order in the nuclear coordinates,

$$S_{\eta\tau}^{\text{el}}(\mathbf{Q}) \simeq S_{\eta\tau}^{\text{el}}(\mathbf{Q}_{\text{eq}}) + \sum_{n=1}^{N_{\text{vib}}} \frac{\partial S_{\eta\tau}^{\text{el}}}{\partial Q_n} \Big|_{\mathbf{Q}=\mathbf{Q}_{\text{eq}}} (Q_n - Q_{n,\text{eq}}) \equiv S_{\eta\tau}^{(0)} + S_{\eta\tau}^{(1)T} \mathbf{Q}, \quad (12)$$

where the ground-state equilibrium geometry is usually referred to, but alternative reference geometries—specifically the excited-state equilibrium geometry—could be appropriate. Inserting this expansion into the expression Eq. (9) for the two-photon transition matrix element yields a sum over FC and HT type terms,

$$S_{\eta\tau} = S_{\eta\tau}^{\text{el}}(\mathbf{Q}_{\text{eq}}) \langle \mathbf{v}_g | \mathbf{v}_e \rangle + \sum_{n=1}^{N_{\text{vib}}} \frac{\partial S_{\eta\tau}^{\text{el}}}{\partial Q_n} \Big|_{\mathbf{Q}=\mathbf{Q}_{\text{eq}}} \langle \mathbf{v}_g | (Q_n - Q_{n,\text{eq}}) | \mathbf{v}_e \rangle \\ = S_{\eta\tau}^{(0)}(\mathbf{Q}_{\text{eq}}) \langle \mathbf{v}_g | \mathbf{v}_e \rangle + \sum_{n=1}^{N_{\text{vib}}} S_{\eta\tau}^{(1,n)} \langle \mathbf{v}_g | (Q_n - Q_{n,\text{eq}}) | \mathbf{v}_e \rangle \\ \equiv S_{\eta\tau}^{\text{FC}} + \sum_n S_{\eta\tau,n}^{\text{HT}}, \quad (13)$$

where the FC term involves the overlap integral $\langle \mathbf{v}_g | \mathbf{v}_e \rangle$ and the HT terms require computation of the coordinate matrix elements $\langle \mathbf{v}_g | Q_n | \mathbf{v}_e \rangle$. If HT contributions are non-negligible, the 2PA transition probability of Eq. (6) will involve cross-terms of various types originating in products of the above transition matrix elements. This gives rise to three types of contributions to each term in the 2PA probability (where we drop the superscript \mathbf{v}_e for convenience),

$$\delta_{2\text{PA}} = \sum_{I \in \{F,G,H\}} I \delta_I = \sum_{I \in \{F,G,H\}} I (\delta_I^{\text{FC}} + \delta_I^{\text{FC,HT}} + \delta_I^{\text{HT}}), \quad (14)$$

where the pure FC term reads

$$\delta_I^{\text{FC}} = S_{\eta\tau}^{\text{FC}} S_{\eta'\tau'}^{\text{FC}*} = S_{\eta\tau}^{(0)} S_{\eta'\tau'}^{(0)*} |\langle \mathbf{v}_g | \mathbf{v}_e \rangle|^2, \quad (15)$$

while the mixed FC/HT terms are given as

$$\delta_I^{\text{FC,HT}} = S_{\eta\tau}^{\text{FC}} \left(\sum_n S_{\eta'\tau',n}^{\text{HT}*} \right) + \left(\sum_n S_{\eta\tau,n}^{\text{HT}} \right) S_{\eta'\tau'}^{\text{FC}*} \\ = \sum_n S_{\eta\tau}^{(0)} S_{\eta'\tau'}^{(1,n)*} \langle \mathbf{v}_g | \mathbf{v}_e \rangle \langle \mathbf{v}_e | (Q_n - Q_{n,\text{eq}}) | \mathbf{v}_g \rangle \\ + \sum_n S_{\eta\tau}^{(1,n)} S_{\eta'\tau'}^{(0)*} \langle \mathbf{v}_g | (Q_n - Q_{n,\text{eq}}) | \mathbf{v}_e \rangle \langle \mathbf{v}_e | \mathbf{v}_g \rangle, \quad (16)$$

and the HT term reads

$$\delta_I^{\text{HT}} = \sum_n \sum_{n'} S_{\eta\tau,n}^{\text{HT}} S_{\eta'\tau',n'}^{\text{HT}*} \\ = \sum_n \sum_{n'} S_{\eta\tau}^{(1,n)} S_{\eta'\tau'}^{(1,n')*} \langle \mathbf{v}_g | (Q_n - Q_{n,\text{eq}}) | \mathbf{v}_e \rangle \\ \times \langle \mathbf{v}_e | (Q_{n'} - Q_{n',\text{eq}}) | \mathbf{v}_g \rangle. \quad (17)$$

Notice that the last term involves cross terms between HT contributions of different nuclear coordinates Q_n .

3. Computation of 2PA cross-section: FCclasses

In order to compute the 2PA cross section of Eq. (4), the time-independent formulation focuses upon the electronic transition matrix elements along with the FC overlap integrals $\langle \mathbf{v}_g | \mathbf{v}_e \rangle$ between the initial and final vibrational states and the HT coordinate matrix elements $\langle \mathbf{v}_g | Q_k | \mathbf{v}_e \rangle$, see Eq. (13). In practice, it turns out that even in medium-sized molecules, the number of possible final vibrational states $|\mathbf{v}_e\rangle$ is so large that the calculation of all FC integrals is not feasible, and a suitable subset must be selected. Here, we follow the *FCclasses* scheme^{17,18} where the vibrational states are partitioned into so-called classes C_n , where n is the number of simultaneously excited normal modes in the final state $|\mathbf{v}_e\rangle$.

Since the number of states in each class grows rapidly with increasing n , approximations are in order. For a spectrum at $T = 0$ K, all integrals, up to sufficiently high maximum quantum numbers, are computed for the first two classes, C_1 and C_2 . Using these data, an iterative procedure determines the best set of quantum numbers for class C_n (up to C_7) under the constraint that the total number of integrals to be computed for each class does not exceed a pre-set maximum number N_{max} . By increasing N_{max} , the method can be converged to arbitrary accuracy.

Spectra from initial states that are vibrationally excited ($|\mathbf{v}_{gk}\rangle$) are computed adopting a modified strategy developed for thermally excited states.²⁰ In these cases, both the C_1 and C_2 transitions from the ground state ($|\mathbf{0}_g\rangle$) and the excited state ($|\mathbf{v}_{gk}\rangle$) are computed and used to select the relevant transitions of higher classes. As one would intuitively expect, excitations of the final-state modes that are most similar to those excited in the initial state are particularly important to reach reasonable convergence of the spectra. Therefore, the subset of final-state modes that project upon the initial-state excited vibrational modes is determined, and, for high classes C_n ($n > n_{\text{max}}$), final vibrational states where these modes are not excited are neglected. Usually, $n_{\text{max}} = 5$ provides a good compromise between accuracy and computational cost.

B. Time-dependent approach

1. General formulation

As in the one-photon case, a complementary time-dependent formulation can be sought by expressing the 2PA cross section of Eq. (4) and Eq. (11) by a Fourier transformation,^{26,27} here adapted

to the Lorentzian line shape function L of Eq. (5), whose Fourier transform (FT) yields an exponential decay with time constant Γ^{-1} ,

$$\begin{aligned} \sigma_{2PA}(\omega) &= \frac{4\pi^3 a_0^5 \alpha}{15c} \omega^2 \sum_{I \in \{F, G, H\}} I \left(\frac{1}{2\pi} \right) \\ &\times \int_{-\infty}^{\infty} dt \sum_{\mathbf{v}_e} \langle \mathbf{v}_g | S_{\eta_1 \tau_1}^{\text{el}} | \mathbf{v}_e \rangle \langle \mathbf{v}_e | S_{\eta_1' \tau_1'}^{\text{el}*} | \mathbf{v}_g \rangle \\ &\times \exp \left[-\frac{i}{\hbar} (\Delta E_{ge} - E_{\mathbf{v}_g} + E_{\mathbf{v}_e} - 2\hbar\omega - i\hbar\Gamma) t \right]. \end{aligned} \quad (18)$$

Next, we note that the above expression contains the excited-state propagator,

$$K_e(t) = e^{-iH_e t/\hbar} = \sum_{\mathbf{v}_e} | \mathbf{v}_e \rangle \exp \left[-\frac{i}{\hbar} E_{\mathbf{v}_e} t \right] \langle \mathbf{v}_e |, \quad (19)$$

and also the operation of the ground-state propagator on the initial stationary vibrational ground state, $\langle \mathbf{v}_g | K_g^\dagger(t) = \langle \mathbf{v}_g | e^{iE_{\mathbf{v}_g} t/\hbar}$. As a result, the above expression can be re-cast as the Fourier transform of correlation functions $\chi_I(t)$,

$$\begin{aligned} \sigma_{2PA}(\omega) &= \frac{4\pi^3 a_0^5 \alpha}{15c} \omega^2 \sum_{I \in \{F, G, H\}} I \left(\frac{1}{2\pi} \right) \int_{-\infty}^{\infty} dt \chi_I(t) \\ &\times \exp \left[-\frac{i}{\hbar} (\Delta E_{ge} - 2\hbar\omega - i\hbar\Gamma) t \right], \end{aligned} \quad (20)$$

where the correlation function $\chi_I(t)$ is given by

$$\begin{aligned} \chi_I(t) &= \langle \mathbf{v}_g | S_{\eta_1 \tau_1}^{\text{el}} K_e(t) S_{\eta_1' \tau_1'}^{\text{el}*} K_g^\dagger(t) | \mathbf{v}_g \rangle \\ &= \text{Tr} \left[S_{\eta_1 \tau_1}^{\text{el}} e^{-iH_e t/\hbar} S_{\eta_1' \tau_1'}^{\text{el}*} e^{iH_g t/\hbar} \rho_g(0) \right], \end{aligned} \quad (21)$$

where Tr denotes the trace operation, and $\rho_g(0)$ is the vibrational density operator referring to the initial state ($| \mathbf{v}_g \rangle$), here $\rho_g(0) = | \mathbf{v}_g \rangle \langle \mathbf{v}_g |$.

Writing the general result of Eq. (20) explicitly for the three contributions $I \in \{F, G, H\}$, we obtain

$$\begin{aligned} \sigma_{2PA}(\omega) &= \frac{4\pi^3 a_0^5 \alpha}{(2\pi)15c} \omega^2 \int_{-\infty}^{\infty} dt e^{-i(\Delta E_{eg} - 2\hbar\omega - i\hbar\Gamma)t/\hbar} \\ &\times (F\chi_F(t) + G\chi_G(t) + H\chi_H(t)). \end{aligned} \quad (22)$$

We further note that each component correlation function can be decomposed into Franck–Condon, Herzberg–Teller, and mixed Franck–Condon/Herzberg–Teller contributions by analogy with Eq. (14) for the 2PA probability,

$$\chi_I(t) = \chi_I^{\text{FC}}(t) + \chi_I^{\text{FC,HT}}(t) + \chi_I^{\text{HT}}(t). \quad (23)$$

The detailed expressions for these components follow from the above derivation and are specified below in the context of the coordinate-domain evaluation of the correlation functions.

More general expressions for the above correlation functions starting from a thermally populated initial state have been discussed elsewhere,^{26,28–35} and analogous correlation functions for a 0 K state have been derived in Ref. 29.

In the following, we derive analytical expressions for these correlation functions within the harmonic approximation. The analytical approach detailed below bears some relation to the developments

in Refs. 29, 36, and 37, where general time-dependent formulations were addressed that also included excitation of selected modes.

2. Excitation from vibrationally pre-excited state: Analytical correlation functions

We now focus on obtaining an explicit expression for the 2PA correlation functions in the case where the initial vibrational state is selectively pre-excited, i.e., the initial state is given as $| \mathbf{v}_g \rangle = | \mathbf{0}_g + \mathbf{1}_{gk} \rangle$, or $\rho_g(0) = | \mathbf{0}_g + \mathbf{1}_{gk} \rangle \langle \mathbf{0}_g + \mathbf{1}_{gk} |$ at $T = 0$ K. The correlation functions then of Eq. (21) take the form

$$\chi_I(t) = e^{iE_{\mathbf{0}_g + \mathbf{1}_{gk}} t/\hbar} \langle \mathbf{0}_g + \mathbf{1}_{gk} | S_{\eta_1 \tau_1}^{\text{el}} K_e(t) S_{\eta_1' \tau_1'}^{\text{el}*} | \mathbf{0}_g + \mathbf{1}_{gk} \rangle, \quad (24)$$

where $E_{\mathbf{0}_g + \mathbf{1}_{gk}}$ is the ground-state energy including pre-excitation. The correlation functions can be evaluated analytically by adopting the coordinate representation for the propagator and the vibrational states, as is sketched out in the following.

In line with the treatment of Refs. 9, 28, 29, and 38, the completeness relation of the initial state normal modes, \mathbf{Q}_g , is used, and the correlation functions are expressed as

$$\begin{aligned} \chi_I(t) &= e^{iE_{\mathbf{0}_g + \mathbf{1}_{gk}} t/\hbar} \int d\tilde{\mathbf{Q}}_g \int d\mathbf{Q}_g \langle \mathbf{0}_g + \mathbf{1}_{gk} | \mathbf{Q}_g \rangle \\ &\times \langle \mathbf{Q}_g | S_{\eta_1 \tau_1}^{\text{el}} K_e(t) S_{\eta_1' \tau_1'}^{\text{el}*} | \tilde{\mathbf{Q}}_g \rangle \langle \tilde{\mathbf{Q}}_g | \mathbf{0}_g + \mathbf{1}_{gk} \rangle. \end{aligned} \quad (25)$$

The coordinate representation of the vibrationally pre-excited initial state is given as follows:

$$\langle \mathbf{Q}_g | \mathbf{0}_g + \mathbf{1}_{gk} \rangle = Q_k (2\Omega_{gk})^{1/2} \langle \mathbf{Q}_g | \mathbf{0}_g \rangle, \quad (26)$$

with the harmonic oscillator ground state

$$\langle \mathbf{Q}_g | \mathbf{0}_g \rangle = \left(\frac{\det(\mathbf{\Omega}_g)}{\pi^N} \right)^{1/4} \exp \left[-\frac{\mathbf{Q}_g^T \mathbf{\Omega}_g \mathbf{Q}_g}{2} \right], \quad (27)$$

where $\mathbf{\Omega}_g$ is a diagonal matrix containing the reduced frequencies of the initial state (g) normal modes $(\mathbf{\Omega}_g)_{kk} = \Omega_{gk} = \omega_{gk}/\hbar$. From Eqs. (26) and (27), we note that $\langle \mathbf{Q}_g | \mathbf{0}_g + \mathbf{1}_{gk} \rangle = \langle \mathbf{0}_g + \mathbf{1}_{gk} | \mathbf{Q}_g \rangle$. Inserting the latter expression into Eq. (25) results in

$$\begin{aligned} \chi_I(t) &= 2\Omega_{gk} e^{iE_{\mathbf{0}_g + \mathbf{1}_{gk}} t/\hbar} \left(\frac{\det(\mathbf{\Omega}_g)}{\pi^N} \right)^{1/2} \int d\tilde{\mathbf{Q}}_g \int d\mathbf{Q}_g Q_{gk} \tilde{Q}_{gk} \\ &\times \exp \left[-\frac{\mathbf{Q}_g^T \mathbf{\Omega}_g \mathbf{Q}_g}{2} \right] \langle \mathbf{Q}_g | S_{\eta_1 \tau_1}^{\text{el}} K_e(t) S_{\eta_1' \tau_1'}^{\text{el}*} | \tilde{\mathbf{Q}}_g \rangle \exp \left[-\frac{\tilde{\mathbf{Q}}_g^T \mathbf{\Omega}_g \tilde{\mathbf{Q}}_g}{2} \right]. \end{aligned} \quad (28)$$

In order to represent the matrix elements of the final state propagator of Eq. (19), $K_e(t)$, it is most convenient to refer to the basis of excited (final) state normal modes \mathbf{Q}_e . Therefore, we now introduce two complete sets of final state coordinates \mathbf{Q}_e ,

$$\begin{aligned} \chi_I(t) &= 2\Omega_{gk} e^{iE_{\mathbf{0}_g + \mathbf{1}_{gk}} t/\hbar} \left(\frac{\det(\mathbf{\Omega}_g)}{\pi^N} \right)^{1/2} \int d\tilde{\mathbf{Q}}_g \int d\mathbf{Q}_g \\ &\times \int d\tilde{\mathbf{Q}}_e \int d\mathbf{Q}_e Q_{gk} \tilde{Q}_{gk} \exp \left[-\frac{\mathbf{Q}_g^T \mathbf{\Omega}_g \mathbf{Q}_g}{2} \right] \\ &\times \langle \mathbf{Q}_g | S_{\eta_1 \tau_1}^{\text{el}} | \mathbf{Q}_e \rangle \langle \mathbf{Q}_e | K_e(t) | \tilde{\mathbf{Q}}_e \rangle \langle \tilde{\mathbf{Q}}_e | S_{\eta_1' \tau_1'}^{\text{el}*} | \tilde{\mathbf{Q}}_g \rangle \exp \left[-\frac{\tilde{\mathbf{Q}}_g^T \mathbf{\Omega}_g \tilde{\mathbf{Q}}_g}{2} \right]. \end{aligned} \quad (29)$$

We can now use Feynman's path integral expression to evaluate the matrix elements of the excited-state propagator Eq. (19),

$$\begin{aligned} \langle \mathbf{Q}_e | K_e(t) | \bar{\mathbf{Q}}_e \rangle &= \left(\frac{\det(\mathbf{a}_e(t))}{(2\pi i \hbar)^N} \right)^{1/2} \\ &\times \exp \left\{ \frac{i}{\hbar} \left[\frac{1}{2} \mathbf{Q}_e^T \mathbf{b}_e(t) \mathbf{Q}_e + \frac{1}{2} \bar{\mathbf{Q}}_e^T \mathbf{b}_e(t) \bar{\mathbf{Q}}_e \right. \right. \\ &\quad \left. \left. - \mathbf{Q}_e^T \mathbf{a}_e(t) \bar{\mathbf{Q}}_e \right] \right\}, \end{aligned} \quad (30)$$

where $\mathbf{a}_e(t)$ and $\mathbf{b}_e(t)$ are diagonal matrices with

$$(\mathbf{a}_e)_{kk}(t) \equiv a_{ek}(t) = \frac{\Omega_{ek}}{\sin(\hbar \Omega_{ek} t)}$$

and

$$(\mathbf{b}_e)_{kk}(t) \equiv b_{ek}(t) = \frac{\Omega_{ek}}{\tan(\hbar \Omega_{ek} t)}. \quad (31)$$

We further have

$$\langle \mathbf{Q}_g | S_{\eta_1 \tau_1}^{\text{el}} | \mathbf{Q}_e \rangle = S_{\eta_1 \tau_1}^{\text{el}}(\mathbf{Q}_g) \delta(\mathbf{Q}_e - \mathbf{J} \mathbf{Q}_g - \mathbf{K}), \quad (32)$$

where we used Eq. (1), and the coordinate dependence of the electronic two-photon transition matrix element will be approximated by the linearized expansion of Eq. (13). Here, the reference geometry is usually chosen as the ground-state equilibrium geometry, such that Eq. (29) is eventually rewritten in terms of ground-state normal-mode coordinates. Hence, Eq. (30) is inserted into Eq. (29), and the integrals over the excited-state coordinates are eliminated using Eq. (32), such as to yield

$$\begin{aligned} \chi_I(t) &= 2\Omega_{gk} e^{iE_{0g} + 1_{gk} t / \hbar} \left(\frac{\det(\mathbf{\Omega}_g)}{\pi^N} \right)^{1/2} \left(\frac{\det(\mathbf{a}_e(t))}{(2\pi i \hbar)^N} \right)^{1/2} \int d\bar{\mathbf{Q}}_g \int d\mathbf{Q}_g Q_{gk} \bar{Q}_{gk} \exp \left[-\frac{\mathbf{Q}_g^T \mathbf{\Omega}_g \mathbf{Q}_g}{2} \right] \\ &\times S_{\eta_1 \tau_1}^{\text{el}}(\mathbf{Q}_g) \exp \left\{ \frac{i}{\hbar} \left[\frac{1}{2} (\mathbf{Q}_g^T \mathbf{J}^T + \mathbf{K}^T) \mathbf{b}_e(t) (\mathbf{J} \mathbf{Q}_g + \mathbf{K}) + \frac{1}{2} (\bar{\mathbf{Q}}_g^T \mathbf{J}^T + \mathbf{K}^T) \mathbf{b}_e(t) (\mathbf{J} \bar{\mathbf{Q}}_g + \mathbf{K}) \right] \right\} \\ &\times \exp \left\{ \frac{i}{\hbar} \left[-(\mathbf{Q}_g^T \mathbf{J}^T + \mathbf{K}^T) \mathbf{a}_e(t) (\mathbf{J} \bar{\mathbf{Q}}_g + \mathbf{K}) \right] \right\} S_{\eta_1 \tau_1}^{\text{el}*}(\bar{\mathbf{Q}}_g) \exp \left[-\frac{\bar{\mathbf{Q}}_g^T \mathbf{\Omega}_g \bar{\mathbf{Q}}_g}{2} \right]. \end{aligned} \quad (33)$$

Re-ordering these terms yields the following:

$$\begin{aligned} \chi_I(t) &= c_0(t) \int d\bar{\mathbf{Q}}_g \int d\mathbf{Q}_g Q_{gk} \bar{Q}_{gk} S_{\eta_1 \tau_1}^{\text{el}}(\mathbf{Q}_g) S_{\eta_1 \tau_1}^{\text{el}*}(\bar{\mathbf{Q}}_g) \\ &\times \exp \left\{ \frac{i}{\hbar} \left[\mathbf{Q}_g^T \mathbf{A}(t) \mathbf{Q}_g + \bar{\mathbf{Q}}_g^T \mathbf{A}(t) \bar{\mathbf{Q}}_g + (\mathbf{Q}_g^T + \bar{\mathbf{Q}}_g^T) \mathbf{B}(t) \mathbf{K} \right. \right. \\ &\quad \left. \left. + \mathbf{K}^T \mathbf{B}^T(t) (\mathbf{Q}_g + \bar{\mathbf{Q}}_g) - \mathbf{Q}_g^T \mathbf{C}(t) \bar{\mathbf{Q}}_g \right] \right\}, \end{aligned} \quad (34)$$

where

$$\begin{aligned} c_0(t) &= 2\Omega_{gk} e^{iE_{0g} + 1_{gk} t / \hbar} \left(\frac{\det(\mathbf{\Omega}_g)}{\pi^N} \right)^{1/2} \left(\frac{\det(\mathbf{a}_e(t))}{(2\pi i \hbar)^N} \right)^{1/2} \\ &\times \exp \left[\frac{i}{\hbar} \mathbf{K}^T (\mathbf{b}_e(t) - \mathbf{a}_e(t)) \mathbf{K} \right], \\ \mathbf{A}(t) &= \frac{1}{2} \left\{ \left(-\frac{\hbar}{i} \right) \mathbf{\Omega}_g + \mathbf{J}^T \mathbf{b}_e(t) \mathbf{J} \right\}, \\ \mathbf{B}(t) &= \frac{1}{2} \mathbf{J}^T (\mathbf{b}_e(t) - \mathbf{a}_e(t)), \\ \mathbf{C}(t) &= \mathbf{J}^T \mathbf{a}_e(t) \mathbf{J}, \end{aligned} \quad (35)$$

where we used the symmetry of the scalar product, $\mathbf{Q}_g^T \mathbf{D} = \mathbf{D}^T \mathbf{Q}_g$, for a real-valued vector \mathbf{D} .

Alternatively, Eq. (34) can be rewritten as

$$\begin{aligned} \chi_I(t) &= c_0(t) \int d\bar{\mathbf{Q}}_g \int d\mathbf{Q}_g Q_{gk} \bar{Q}_{gk} S_{\eta_1 \tau_1}^{\text{el}}(\mathbf{Q}_g) S_{\eta_1 \tau_1}^{\text{el}*}(\bar{\mathbf{Q}}_g) \\ &\times \mathcal{F}(\mathbf{Q}_g, \bar{\mathbf{Q}}_g; \mathbf{A}(t), \mathbf{B}(t), \mathbf{C}(t)), \end{aligned} \quad (36)$$

where $\mathcal{F}(\mathbf{Q}_g, \bar{\mathbf{Q}}_g; \mathbf{A}(t), \mathbf{B}(t), \mathbf{C}(t))$ is a quadratic form,

$$\begin{aligned} \mathcal{F}(\mathbf{Q}_g, \bar{\mathbf{Q}}_g; \mathbf{A}(t), \mathbf{B}(t), \mathbf{C}(t)) \\ = \mathcal{G}(\mathbf{Q}_g; \mathbf{A}(t), \mathbf{B}(t)) \mathcal{G}(\bar{\mathbf{Q}}_g; \mathbf{A}(t), \mathbf{B}(t)) \mathcal{C}(\mathbf{Q}_g, \bar{\mathbf{Q}}_g; \mathbf{C}(t)), \end{aligned} \quad (37)$$

$$\begin{aligned} \mathcal{G}(\mathbf{Q}_g; \mathbf{A}(t), \mathbf{B}(t)) &= \exp \left\{ \frac{i}{\hbar} \left[\mathbf{Q}_g^T \mathbf{A}(t) \mathbf{Q}_g + \mathbf{Q}_g^T \mathbf{B}(t) \mathbf{K} \right. \right. \\ &\quad \left. \left. + \mathbf{K}^T \mathbf{B}^T(t) \mathbf{Q}_g \right] \right\} \end{aligned} \quad (38)$$

$$\mathcal{C}(\mathbf{Q}_g, \bar{\mathbf{Q}}_g; \mathbf{C}(t)) = \exp \left\{ -\frac{i}{\hbar} \mathbf{Q}_g^T \mathbf{C}(t) \bar{\mathbf{Q}}_g \right\},$$

and the expression for $\mathcal{G}(\bar{\mathbf{Q}}_g; \mathbf{A}(t), \mathbf{B}(t))$ is analogous to $\mathcal{G}(\mathbf{Q}_g; \mathbf{A}(t), \mathbf{B}(t))$.

Inserting the linearized expansion for the transition moments according to Eq. (12),

$$\begin{aligned} \chi_I(t) &= c_0(t) \int d\bar{\mathbf{Q}}_g \int d\mathbf{Q}_g Q_{gk} \bar{Q}_{gk} \left(S_{\eta_1 \tau_1}^{(0)} + S_{\eta_1 \tau_1}^{(1)T} \mathbf{Q}_g \right) \\ &\times \left(S_{\eta_1 \tau_1}^{(0)*} + S_{\eta_1 \tau_1}^{(1)*T} \bar{\mathbf{Q}}_g \right) \mathcal{F}(\mathbf{Q}_g, \bar{\mathbf{Q}}_g; \mathbf{A}(t), \mathbf{B}(t), \mathbf{C}(t)), \end{aligned} \quad (39)$$

three types of contributions are obtained, involving the FC terms (from the zeroth-order terms $S_{\eta_1 \tau_1}^{(0)}$ and $S_{\eta_1 \tau_1}^{(0)*}$), mixed FC/HT terms (from combinations of the $S_{\eta_1 \tau_1}^{(0)}$ and $S_{\eta_1 \tau_1}^{(1)}$ terms and the complementary $S_{\eta_1 \tau_1}^{(1)*}$ and $S_{\eta_1 \tau_1}^{(0)*}$ terms) and HT terms (from the $S_{\eta_1 \tau_1}^{(1)}$ and $S_{\eta_1 \tau_1}^{(1)*}$ combination), leading to the sum of terms introduced in Eq. (23),

$$\chi_I(t) = \chi_I^{\text{FC}}(t) + \chi_I^{\text{FC,HT}}(t) + \chi_I^{\text{HT}}(t), \quad (40)$$

where

$$\begin{aligned}\chi_I^{\text{FC}}(t) &= c_0(t) S_{\eta_i \tau_i}^{(0)} S_{\eta_i' \tau_i'}^{(0)*} M^{(1_k \bar{1}_k)}(t) \\ \chi_I^{\text{FC,HT}}(t) &= c_0(t) \left(S_{\eta_i \tau_i}^{(0)} \left(S_{\eta_i' \tau_i'}^{(1)*T} \mathbf{M}^{(1_k \bar{2}_{k,N})}(t) \right) \right. \\ &\quad \left. + \left(S_{\eta_i \tau_i}^{(1)T} \mathbf{M}^{(2_{k,N} \bar{1}_k)}(t) \right) S_{\eta_i' \tau_i'}^{(0)*} \right) \\ \chi_I^{\text{HT}}(t) &= c_0(t) S_{\eta_i \tau_i}^{(1)T} \mathbf{M}^{(2_{k,N} \bar{2}_{k,N})}(t) S_{\eta_i' \tau_i'}^{(1)*},\end{aligned}\quad (41)$$

with the Gaussian moments

$$\begin{aligned}M^{(1_k \bar{1}_k)}(t) &= \int d\tilde{\mathbf{Q}}_g \int d\mathbf{Q}_g Q_{gk} \tilde{Q}_{gk} \\ &\quad \times \mathcal{F}(\mathbf{Q}_g, \tilde{\mathbf{Q}}_g; \mathbf{A}(t), \mathbf{B}(t), \mathbf{C}(t)) \\ \mathbf{M}^{(1_k \bar{2}_{k,N})}(t) &= \int d\tilde{\mathbf{Q}}_g \int d\mathbf{Q}_g Q_{gk} \tilde{Q}_{gk} \tilde{\mathbf{Q}}_g \\ &\quad \times \mathcal{F}(\mathbf{Q}_g, \tilde{\mathbf{Q}}_g; \mathbf{A}(t), \mathbf{B}(t), \mathbf{C}(t)) \\ \mathbf{M}^{(2_{k,N} \bar{2}_{k,N})}(t) &= \int d\tilde{\mathbf{Q}}_g \int d\mathbf{Q}_g Q_{gk} \tilde{Q}_{gk} \mathbf{Q}_g \tilde{\mathbf{Q}}_g^T \\ &\quad \times \mathcal{F}(\mathbf{Q}_g, \tilde{\mathbf{Q}}_g; \mathbf{A}(t), \mathbf{B}(t), \mathbf{C}(t)),\end{aligned}\quad (42)$$

where $M^{(1_k \bar{1}_k)}$ is a scalar second-order moment, $\mathbf{M}^{(1_k \bar{2}_{k,N})}$ and $\mathbf{M}^{(2_{k,N} \bar{1}_k)}$ are vectors of third-order moments, and $\mathbf{M}^{(2_{k,N} \bar{2}_{k,N})}$ is a matrix of fourth-order moments. In all moments, two coordinates are fixed to the pre-excited mode (Q_{gk} , \tilde{Q}_{gk}) while the other coordinates involve all normal modes participating in the HT terms. These multivariate Gaussian moments can be integrated analytically, e.g., using generating function methods.³⁶

In Ref. 9, we carried out TD and TI analyses for the analogous one-photon (1P-VIPER) experiment; however, HT contributions were not included. When accounting for both FC and HT contributions, the relevant expressions for the correlation functions would entirely correspond to Eqs. (40)–(42), upon replacing the two-photon transition moments by the corresponding transition dipole moments.

In the [supplementary material](#) (part II), a complementary formulation for the 2P-VIPER correlation functions is detailed, which initially casts the above expressions in terms of integrals over the excited-state normal modes, permitting for back-transformation to ground-state normal modes at a later stage. Analogous final expressions for the 1P-VIPER case, including both FC and HT terms, are also reported. This approach is employed in the *FCclasses3* implementation.^{17–19}

C. Two-photon VIPER enhancement

In our earlier study of one-photon VIPER spectroscopy,⁹ we obtained an approximate *a priori* estimate of the suitability of a particular normal mode for VIPER excitation, by computing the ratio of the transition moments from the pre-excited vibrational state $|\mathbf{0}_g + 1_{gk}\rangle$ vs the ground vibrational state $|\mathbf{0}_g\rangle$ to the ground vibrational state of the excited electronic state $|\mathbf{0}_e\rangle$. When neglecting Duschinsky effects, a simple result is obtained,⁹

$$\mathcal{E}_{1\text{P}}^{\text{FC},k} = \frac{\langle \mathbf{0}_g + 1_{gk} | \mathbf{0}_e \rangle}{\langle \mathbf{0}_g | \mathbf{0}_e \rangle} = \frac{d_k}{\sqrt{2}},\quad (43)$$

where \mathbf{d} is the vector of the dimensionless displacements along the ground state normal modes, obtained from the mass-weighted displacement vector \mathbf{K} according to the transformation $\mathbf{d} = (\mathbf{K}')^T \boldsymbol{\Omega}_g^{1/2} = -(\mathbf{J}^T \mathbf{K})^T \boldsymbol{\Omega}_g^{1/2}$. The \mathbf{d} displacements, which are related to the Huang–Rhys factors (i.e., $S_k^{\text{HR}} = \frac{1}{2} d_k^2$),³⁹ are a useful quantity for determining the difference between the two states' equilibrium structures. In Ref. 9, the above result was further extended, such as to include Duschinsky rotation effects.

While we expect the above FC enhancement to carry over to the 2P case [see Eq. (47) below], Herzberg–Teller effects should also play a non-negligible role in the context of the present two-photon study. In contrast, HT effects were not considered in our previous one-photon study due to their minimal influence.⁹ Hence, the 2P-VIPER enhancement will also encompass HT contributions, where we consider again transitions between the states $|\mathbf{v}_g\rangle = |\mathbf{0}_g + 1_{gk}\rangle$ and $|\mathbf{v}_e\rangle = |\mathbf{0}_e\rangle$, as compared to the 0–0 transition between $|\mathbf{v}_g\rangle = |\mathbf{0}_g\rangle$ and $|\mathbf{v}_e\rangle = |\mathbf{0}_e\rangle$, just as in the FC case,

$$\left(\mathcal{E}_{2\text{P}}^{\text{FC},k} \right)_{\eta\tau} = \frac{S_{\eta\tau}^{(0)} \langle \mathbf{0}_g + 1_{gk} | \mathbf{0}_e \rangle}{S_{\eta\tau}^{(0)} \langle \mathbf{0}_g | \mathbf{0}_e \rangle}\quad (44)$$

and

$$\left(\mathcal{E}_{2\text{P}}^{\text{HT},k} \right)_{\eta\tau} = \frac{\sum_n S_{\eta\tau}^{(1,n)} \langle \mathbf{0}_g + 1_{gk} | Q_n | \mathbf{0}_e \rangle}{\sum_n S_{\eta\tau}^{(1,n)} \langle \mathbf{0}_g | Q_n | \mathbf{0}_e \rangle}.\quad (45)$$

However, Eq. (45) for the HT enhancement is a delicate quantity since the 0–0 transition may not be a suitable reference. For instance, for a symmetric molecular species, HT effects are induced by non-totally symmetric modes, for which the 0–0 transition exhibits zero intensity such that the denominator in Eq. (45) vanishes. These limitations should be kept in mind in the following discussion.

The HT expression of Eq. (45) necessitates distinguishing between the cases $n = k$ and $n \neq k$, i.e., such that HT effects are considered for the pre-excited mode k or for one of the other modes,

$$\left(\mathcal{E}_{2\text{P}}^{\text{HT},k} \right)_{\eta\tau} = \frac{S_{\eta\tau}^{(1,k)} \langle \mathbf{0}_g + 1_{gk} | Q_k | \mathbf{0}_e \rangle + \sum_{n \neq k} S_{\eta\tau}^{(1,n)} \langle \mathbf{0}_g + 1_{gk} | Q_n | \mathbf{0}_e \rangle}{S_{\eta\tau}^{(1,k)} \langle \mathbf{0}_g | Q_k | \mathbf{0}_e \rangle + \sum_{n \neq k} S_{\eta\tau}^{(1,n)} \langle \mathbf{0}_g | Q_n | \mathbf{0}_e \rangle}.\quad (46)$$

Within similar approximations as in Ref. 9, i.e., neglecting Duschinsky effects as in the one-photon FC case of Eq. (43), explicit expressions can be obtained for the above integrals, resulting in the following for the FC contribution:

$$\mathcal{E}_{2\text{P}}^{\text{FC},k} = \frac{d_k}{\sqrt{2}},\quad (47)$$

where we used the relation $\langle 1_{gk} | \mathbf{0}_{ek} \rangle = (d_k / \sqrt{2}) \langle 0_{gk} | \mathbf{0}_{ek} \rangle$, yielding the same result as in the 1P case, see Eq. (43). For the HT contribution, one obtains

$$\left(\mathcal{E}_{2\text{P}}^{\text{HT},k} \right)_{\eta\tau} = \frac{S_{\eta\tau}^{(1,k)} (1 + d_k^2/2) + \sum_{n \neq k} S_{\eta\tau}^{(1,n)} d_k d_n / 2}{S_{\eta\tau}^{(1,k)} d_k / \sqrt{2} + \sum_{n \neq k} S_{\eta\tau}^{(1,n)} d_n / \sqrt{2}},\quad (48)$$

where we further used $\langle 0_{gk} | Q_k | \mathbf{0}_{ek} \rangle = (d_k/2) \langle 0_{gk} | \mathbf{0}_{ek} \rangle$ and $\langle 1_{gk} | Q_k | \mathbf{0}_{ek} \rangle = (1/\sqrt{2})(1 + d_k^2/2) \langle 0_{gk} | \mathbf{0}_{ek} \rangle$. The above expression

highlights that the HT enhancement represents the sum of multiple contributions of different sign and magnitude. If the VIPER-active mode k exhibits a dominant HT effect, i.e., $|S_{\eta\tau}^{(1,k)}| \gg |S_{\eta\tau}^{(1,n)}|$, $n \neq k$, one obtains the following expression, disregarding the remaining modes:

$$\mathcal{E}_{2P}^{\text{HT},k} = \frac{\sqrt{2}(1 + d_k^2/2)}{d_k}. \quad (49)$$

Interestingly, in this limit, the enhancement no longer depends on the derivative $S_{\eta\tau}^{(1,k)}$, i.e., the strength of the HT effect. This expression shows that a large enhancement can be observed for small displacements d_k , while large displacements lead to an enhancement

that is equivalent to the FC enhancement $\mathcal{E}_{2P}^{\text{FC},k}$. In systems where a symmetry classification is appropriate, these cases typically relate to non-totally symmetric modes (with a negligible displacement) vs totally symmetric modes (with a non-negligible displacement). In the former case, i.e., for non-totally symmetric modes, an infinite enhancement results for $d_k \rightarrow 0$. However, in a polyatomic system, multi-mode contributions will appear according to Eq. (46), such that the denominator will take a finite value and the resulting enhancement will be large—but not infinite—in cases, where the VIPER-active mode k shows a dominant contribution.

At the same level of treatment, we can consider both FC and HT effects, such as to obtain the enhancement

$$\left(\mathcal{E}_{2P}^k\right)_{\eta\tau} = \frac{S_{\eta\tau}^{(0)} \langle \mathbf{0}_g + 1_{gk} | \mathbf{0}_e \rangle + S_{\eta\tau}^{(1,k)} \langle \mathbf{0}_g + 1_{gk} | Q_k | \mathbf{0}_e \rangle + \sum_{n \neq k} S_{\eta\tau}^{(1,n)} \langle \mathbf{0}_g + 1_{gk} | Q_n | \mathbf{0}_e \rangle}{S_{\eta\tau}^{(0)} \langle \mathbf{0}_g | \mathbf{0}_e \rangle + S_{\eta\tau}^{(1,k)} \langle \mathbf{0}_g | Q_k | \mathbf{0}_e \rangle + \sum_{n \neq k} S_{\eta\tau}^{(1,n)} \langle \mathbf{0}_g | Q_n | \mathbf{0}_e \rangle}, \quad (50)$$

resulting in the explicit expression

$$\left(\mathcal{E}_{2P}^k\right)_{\eta\tau} = \frac{S_{\eta\tau}^{(0)} d_k + S_{\eta\tau}^{(1,k)} (1 + d_k^2/2) + \sum_{n \neq k} S_{\eta\tau}^{(1,n)} d_k d_n / 2}{\sqrt{2} S_{\eta\tau}^{(0)} + S_{\eta\tau}^{(1,k)} d_k / \sqrt{2} + \sum_{n \neq k} S_{\eta\tau}^{(1,n)} d_n / \sqrt{2}}. \quad (51)$$

Again, a limiting situation can be considered, where the contributions from the pre-excited mode k dominate,

$$\left(\mathcal{E}_{2P}^k\right)_{\eta\tau} = \frac{S_{\eta\tau}^{(0)} d_k + S_{\eta\tau}^{(1,k)} (1 + d_k^2/2)}{\sqrt{2} S_{\eta\tau}^{(0)} + S_{\eta\tau}^{(1,k)} d_k / \sqrt{2}} \quad (52)$$

noting that due to the summations, the enhancement depends in a non-trivial way on the sign of the displacements multiplying $S_{\eta\tau}^{(0)}$ and its derivative $S_{\eta\tau}^{(1,k)}$.

In Table III, we illustrate the above expressions for the $S_{\eta\tau} = S_{xx}$ two-photon transition matrix element, which is found to be by far dominant in the case of Coumarin 6 (see Sec. S3 of the supplementary material). Here, we also report squared enhancements $|(\mathcal{E}_{2P}^{\text{FC},k})_{xx}|^2$, $|(\mathcal{E}_{2P}^{\text{HT},k})_{xx}|^2$, and $|(\mathcal{E}_{2P}^k)_{xx}|^2$, which are representative of the enhancements obtained for the spectral intensities in terms of Eqs. (4)–(7). It is seen from Table III that the estimated HT enhancement is much larger than the FC enhancement, but the combined FC/HT enhancement is again of the same order as the FC enhancement. Clearly, the FC and HT contributions are not additive, and FC/HT interference plays a key role. In the general case, the enhancements would be constructed in terms of the spectral intensities of Eqs. (4)–(7) encompassing products of transition moments that generate a variety of FC/HT cross-terms.

To summarize, while the pure FC expressions, in the absence of HT effects, are identical for one-photon and two-photon absorption, the enhancement effect is considerably complicated by the HT participation, due to the intrinsic multi-mode effect of the HT contributions and due to FC/HT interference.

Finally, we note that we did not include Duschinsky rotation effects in the above considerations, which would complicate the picture due to the coordinate mixing. Hence, the present expressions provide useful trends but not a quantitative analysis.

III. EXPERIMENTAL AND COMPUTATIONAL PROCEDURES

A. Sample preparation and steady-state measurements

Coumarin 6 was purchased from Sigma-Aldrich, Germany, and was used as received and dissolved in tetrahydrofuran (THF, 99.9% Sigma-Aldrich). The Coumarin 6 sample (30 mM) was filled in a flow cell with an optical path length of 250 μm .⁴⁰ The FTIR spectra were recorded on a Tensor 27 spectrometer (Bruker Optics) equipped with a mercury cadmium telluride (MCT) detector (InfraRed Associates Inc, USA).

B. Details of the experimental setup for one- and two-photon VIPER

The one- and two-photon VIPER measurements were carried out using a setup that consisted of a femtosecond oscillator (Tsunami, Spectra-Physics, Newport, USA), which seeded a Ti:Sapphire regenerative amplifier (3.5 mJ, 800 nm, 90 fs, 1 kHz, Spitfire XP, Spectra-Physics, Newport, USA), which was used to pump three home-built optical parametric amplifiers (OPAs).⁴¹ The output of one OPA was used to generate mid-IR probe pulses centered at 1650 cm^{-1} by difference-frequency generation of the OPA's signal and idler pulses in a silver thiogallate crystal (AgGaS_2). Half of the probe light was used as a reference beam. For one photon VIPER, the second OPA generated VIS pulses [495 nm with a full width at half maximum (FWHM) of 2.7 nm; 0.75 μJ /pulse; focus size 110 \times 140 μm^2] by mixing the fundamental of the laser and the signal of the OPA in a BBO crystal. For two-photon VIPER, the second OPA generated the NIR pump pulses (960 nm FWHM 16 nm; 7.4 μJ /pulse; focus size 140 \times 150 μm^2) by doubling the OPA's idler

in a second BBO crystal. The output of the third OPA (centered at 1650 cm^{-1} with a FWHM of 150 cm^{-1} ; $7.3\text{ }\mu\text{J/pulse}$) was sent into a Mach–Zehnder interferometer to generate a pulse pair with a variable delay τ .⁴² The Fourier transform of the time-domain signal as a function of τ yields the pump axis of the 2D-IR spectrum. A mechanical chopper in the VIS or NIR beam was used to measure the Fourier transform two-dimensional (FT-2D) IR spectrum with and without the VIS or NIR beam. The difference between these two spectra produced the VIPER FT 2D-IR spectra.⁵ These spectra were averaged for 3 600 000 laser shots corresponding to $\sim 1\text{ h}$ of measurement time. The probe and reference beams both go through the sample and were dispersed by the same spectrometer (100 lines/mm grating, TRIAX 190, HORIBA Scientific Instruments, USA) and collected by a 2×32 pixel MCT detector (Infrared Associates, USA). The detector dewar was cooled by liquid nitrogen using an automatic, home-built nitrogen refilling system.⁴³ The temporal delays between the IR pump pulse pair and the IR probe pulse, and the NIR or VIS pump pulse and the IR pump pulse were controlled by two motorized linear stages (Physik Instrumente, Germany). For assessing the VIPER effect of the different modes, the delay between the last IR pump pulse and the VIS or NIR pump pulse was 0.7 ps, and the delay between the VIS or NIR pump pulse and the IR probe pulse was 200 ps. The relative polarization of the IR pump beam was magic angle with respect to the NIR/VIS pump beam and perpendicular with respect to the IR probe beam.

To prevent degradation of the sample, a large volume (4 ml) was continuously circulated with the help of a micro annular gear pump (mzr-2942 pump, HNP Microsystems GmbH, Germany). The flow cell ($150\text{ }\mu\text{m}$) was also continuously moved up and down.

C. Computational details

Electronic structure calculations were performed using density functional theory (DFT) and time-dependent density functional theory (TD-DFT) for excited state calculations, as implemented in the Gaussian16 package revision B.01⁴⁴ and the Dalton2018.0 package.²⁵ The B3LYP functional^{45,46} and the def2-TZVP basis set^{47,48} were employed, and comparative calculations were carried out with the CAM-B3LYP functional.⁴⁹ In our previous one-photon study of Coumarin 6,⁹ we employed the long-range-corrected hybrid functional $\omega\text{B97X-D}$;⁵⁰ however, in the present investigation, we were limited in the choice of functionals since these are required to be compatible with the computation of 2P properties using the Dalton code.²⁵ In the [supplementary material](#) (Sec. S2), different DFT functionals and basis sets are addressed, showing that differences between functionals can be quite pronounced as far as excitation energies and two-photon properties are concerned. However, differences between basis sets are generally less pronounced, and the chosen def2-TZVP (triple-zeta polarization) basis set should be considered adequate.

Geometry optimization of the ground and excited states and a harmonic frequency analysis of both were performed employing analytical first and second derivatives. All calculations were carried out using tight optimization criteria as well as a fine integration grid. The solvent effects of THF were accounted for by the Polarizable Continuum Model (PCM).^{51,52} In order to compute the 2P transition moment and 2P absorption

spectra, quadratic response calculations using the same functional and solvent conditions were carried out at the FC geometry employing the Dalton2018.0 program package.²⁵ Numerical differentiation of the 2P transition moment yielded the respective derivatives that were subsequently transformed to ground-state normal mode coordinates.

The harmonic approximation to the ground and excited-state potential energy surface (PES) was expanded around the minimum of the respective state employing the adiabatic Hessian (AH) approach. Vibrationally resolved absorption spectra using 2P excitation were obtained using the *FCclasses3* code.^{18,19} Analogously to the 1P case, all spectra using the time-independent formalism were obtained with $N_{\text{max}} = 10^8$ and subsequently convoluted with a Lorentzian line shape with a half width at half maximum (HWHM) of 0.1 eV. Complementary time-dependent vibrationally resolved spectra were obtained through the analytical correlation function approach (see Sec. II B 2) implemented in the same *FCclasses3* code.

IV. EXPERIMENTAL AND COMPUTATIONAL RESULTS

A. Electronic structure aspects and vibronic effects

Here, a brief account of the electronic structure properties of the Coumarin 6 system, along with one- and two-photon absorption cross sections of the first few singlet states, is given. Our study focuses on the S_1 state, which represents a bright HOMO–LUMO one-photon transition with $\pi\text{--}\pi^*$ character. This is the transition which we previously investigated in a combined experimental and theoretical study using 1P-VIPER excitation.⁹ However, we note that the S_1 state, which exhibits a dominant oscillator strength ($f \sim 1$) shows only moderate two-photon activity (from $\sigma_{2P} \sim 6\text{ GM}$ to $\sigma_{2P} \sim 76\text{ GM}$ depending on the DFT functional and solvent, see [Table I](#)). In contrast, the S_3 state (B3LYP) [S_4 in CAM-B3LYP] is the dominant two-photon state (ranging from $\sigma_{2P} \sim 800\text{ GM}$ to $\sigma_{2P} \sim 1600\text{ GM}$). Even so, the present study focuses on the $S_1 \leftarrow S_0$ transition observed in the 2P-VIPER experiments as reported below in view of the comparison with the 1P-VIPER excitation of the same system [see the illustration in [Fig. 2\(b\)](#)].

[Table I](#) summarizes the 1P and 2P transitions to the first few singlet states computed with the B3LYP functional, while the [supplementary material](#) (Sec. S1) provides details on the relevant orbital transitions and the comparison between the B3LYP vs CAM-B3LYP functionals. As already mentioned, functionals need to be chosen so as to be compatible with the 2P transition moment computation in Dalton (see above). The energetic differences between representative functionals, here B3LYP vs CAM-B3LYP (see [Table I](#)), are non-negligible—of the order of 0.4 eV for the S_1 state and larger for the higher excited states. Apart from this, the electronic structure description is consistent, especially for the S_1 state, whose electronic structure is comparatively simple, as a HOMO–LUMO transition of an extended π system.

The Coumarin 6 molecule contains 43 atoms and, hence, 123 vibrational normal modes. The vibronic absorption spectrum therefore features densely distributed transitions, with some dominant progressions exhibiting spacings of $\sim 0.2\text{ eV}$. These are due to several modes, notably ring distortion modes, henceforth denoted RM1 and RM2, and the CO stretching mode, whose frequencies are listed in [Table II](#). One of these modes, i.e., the ring mode RM1, exhibits

TABLE I. Comparison between the functionals B3LYP and CAM-B3LYP for the lowest four singlet excited states of Coumarin 6. Calculations are, respectively, carried out in vacuum as well as including the solvent effects of THF using a PCM description. Listed are the excitation energy in eV, the respective oscillator strength (f), and the 2P cross-section σ_{2P} in GM.

Solvent/functional		S_1 (HOMO \rightarrow LUMO)	S_2	S_3	S_4
Vacuum/B3LYP	Energy (eV)	3.075	3.514	3.920	4.048
	Oscillator strength f	1.061	0.026	0.006	0.004
	σ_{2P} (GM)	5.59	5.14	846	3.21
Vacuum/CAM-B3LYP	Energy (eV)	3.475	4.428	4.519	4.730
	Oscillator strength f	1.156	0.021	0.031	0.006
	σ_{2P} (GM)	24.1	2.37	4.62	734
THF/B3LYP	Energy (eV)	2.774	3.635	3.877	3.995
	Oscillator strength f	1.437	0.026	0.006	0.018
	σ_{2P} (GM)	42.9	37.3	1570	43.7
THF/CAM-B3LYP	Energy (eV)	3.139	4.439	4.518	4.601
	Oscillator strength f	1.496	0.044	0.098	0.028
	σ_{2P} (GM)	76.4	1.28	19.0	993

a dominant Huang–Rhys factor ($S_{\text{RM1}}^{\text{HR}} \sim 0.1$), while the other ring mode shows a smaller value ($S_{\text{RM2}}^{\text{HR}} \sim 0.01$), as does the CO stretching mode ($S_{\text{CO}}^{\text{HR}} \sim 0.003$), see Table III. As previously shown in our 1P-VIPER analysis,⁹ the ring modes play a prominent role as far as their VIPER activity is concerned. In the present work, we also focus on these modes, along with the CO mode, in view of a comparison with 1P-VIPER. Since the HT effects are included in the two-photon analysis, numerical derivatives of the 2PA cross section are computed along these relevant modes (RM1, RM2, and CO), as reported in the [supplementary material](#), Sec. S3.

B. Experimental 1P-VIPER and 2P-VIPER spectra

As described in Sec. III B, the 2P-VIPER experiment illustrated in Fig. 1 is initiated by a pair of IR pulses separated by a variable

delay τ , which yields the ω_{pump} axis by Fourier transformation. Following IR pre-excitation by these initial pulses, an off-resonant actinic pulse triggers photo-excitation of the subset of molecular species that have experienced IR pre-excitation. The actinic pulse is either a NIR pulse inducing a 2P transition or else a UV/VIS pulse inducing a 1P transition. A comparison between 2P-VIPER and 1P-VIPER experiments is carried out, relying on exactly the same set-up except for the NIR vs UV/VIS nature of the actinic pulse. These new 1P-VIPER experiments for Coumarin 6 supersede our earlier experiments reported in Ref. 9, which were conducted with a Fabry–Pérot interferometer to generate a single, narrow-band IR pulse that was scanned in the frequency domain. In the new FT-based experiments, a much better resolution in the ω_{pump} domain is achieved, and intramolecular vibrational redistribution (IVR) effects are expected to be significantly reduced because

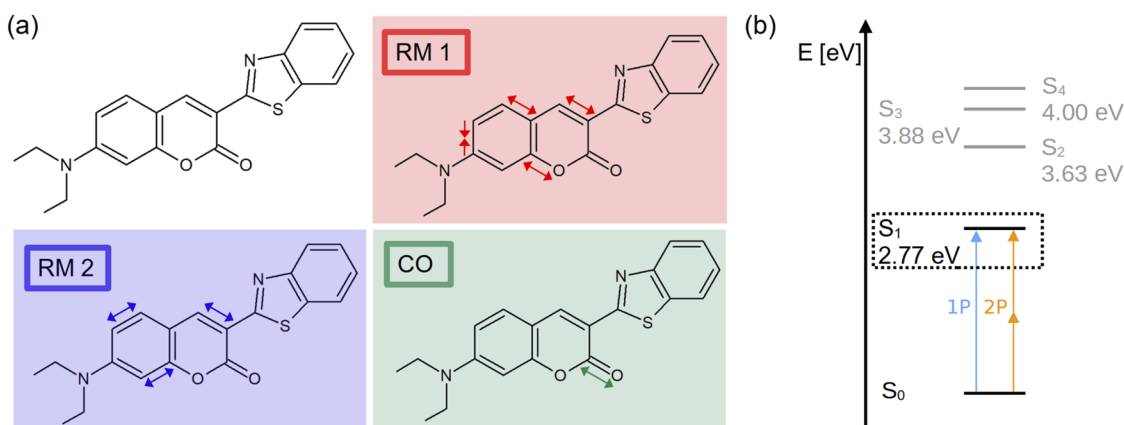
**FIG. 2.** (a) Structure of Coumarin 6 and schematic representation of the dominant normal modes considered in our analysis, i.e., two ring distortion modes, the lower-frequency mode being referred to as RM1 while the higher-frequency mode is denoted RM2, along with a carbonyl stretch mode (CO), see Table II for the relevant vibrational frequencies. (b) Energy level diagram showing the ground state and lowest-lying singlet excited states of Coumarin 6. The electronic transition under consideration is the $S_1 \leftarrow S_0$ transition, for which 1P-VIPER and 2P-VIPER experiments are compared.

TABLE II. Comparison of experimental and computed frequencies in cm^{-1} of the two ring modes and the CO stretch mode of Coumarin 6 using B3LYP and CAM-B3LYP. Experimental frequencies were obtained in THF, and computationally solvent effects of THF were accounted for by the PCM solvation model.

Method	$\nu_{\text{RM1}} (\text{cm}^{-1})$		$\nu_{\text{RM2}} (\text{cm}^{-1})$		$\nu_{\text{CO}} (\text{cm}^{-1})$	
	B3LYP	CAM-B3LYP	B3LYP	CAM-B3LYP	B3LYP	CAM-B3LYP
DFT/vacuum	1624.6	1672.9	1658.0	1695.9	1776.6	1820.1
DFT/THF	1607.5	1647.8	1647.9	1684.9	1730.5	1772.2
Expt.	1596.1		1631.6		1724.0	

the delay t_1 between vibrational and electronic excitation is kept shorter as compared with a spectrally narrow but long IR pump pulse.

In Fig. 3, experimental FT-2D VIPER spectra of Coumarin 6 are shown for one-photon excitation and two-photon excitation. Complementary to the 2D spectra shown in panels (a) and (c), one-dimensional slices along the probe axis are shown in panels (b) and (d), at the frequencies of the RM1, RM2, and CO modes where dominant signals occur, as well as at an off-resonant frequency, to judge the data quality.

It is seen that the 1P-VIPER spectra exhibit a dominant signal for one of the ring modes (RM1). This mode also gives rise to the strongest signal in the 2P-VIPER spectrum, but the intensity of the RM2 and CO modes is also non-negligible in this case.

One should note that the 1P-VIPER spectrum differs to some extent from the spectrum which was previously reported in Ref. 9. Here, the relative VIPER signal generated by excitation of the RM2 mode appeared larger—even though inferior to RM1—which we attribute to the lower resolution along the pump axis in these previous experiments.⁹ It is also noteworthy that the FT approach allows for a shorter delay between the IR pump pulses and the UV or NIR pump pulses as compared to the Fabry–Pérot approach (i.e., 0.7 vs 1.2 ps), therefore less IVR will take place.

In the following, we will explore the theoretical interpretation of these spectra, using the TI and TD approaches detailed above. From the different intensity distributions of the 1P-VIPER vs 2P-VIPER spectra, we can infer that an analysis at the FC level is not sufficient. Differently from our previous analysis⁹, which was restricted to the FC level, we now carry out an analysis for the

2P-VIPER spectra, which also comprises HT contributions as discussed above. The analysis of the 1P-VIPER spectra remains at the FC level since the HT contributions are negligible in this case (see Sec. S4 of the [supplementary material](#)).

C. VIPER pre-excitation: Analysis for selected modes

In Fig. 4, we show theoretical vibronic 2PA spectra without and with pre-excitation, computed with the TI vs TD methods as described above. Pre-excitation leads to a red-shifted absorption feature, visible in panels (b)–(d) and highlighted in the insets. The spectrum in the absence of pre-excitation [panel (a)] is nearly identical to the spectrum shown in our earlier 1P-VIPER study,⁹ where a different DFT functional (i.e., the ω B97X-D functional) was employed. The TI and TD approaches are in close agreement in the range around -2000 to 3000 cm^{-1} (where the origin of the frequency axis is fixed at the 0–0 transition in the absence of vibrational pre-excitation), but deviations are observed at higher energies. As discussed in our previous study,⁹ the TI calculations tend to exhibit reduced intensity due to the truncation effect in the *FC* classes approach, such that the cumulative effect of a large number of small contributions in the high-frequency range is not entirely accounted for. With a threshold of $N_{\text{max}} = 10^8$, as in our previous study,⁹ 94% of the total intensity is recovered for the spectrum without pre-excitation [panel (a)], while the spectra including pre-excitation exhibit more significant loss effects, due to the larger number of accessible excitation pathways that are subject to truncation in the TI approach. By contrast, the TD calculation is exact within the harmonic approximation; therefore, we focus on the TD results in the following discussion.

TABLE III. Dimensionless displacements along the ground state normal modes (d_k), Huang–Rhys factors ($S_k^{\text{HR}} = d_k^2/2$), and 2P-VIPER enhancements computed for the S_{xx} transition element, which is dominant in the case of Coumarin 6. For the 2P-VIPER enhancements, pure FC ($\mathcal{E}_{2\text{P}}^{\text{FC},k}$) and pure HT ($\mathcal{E}_{2\text{P}}^{\text{HT},k}$) terms, as well as the overall enhancement ($\mathcal{E}_{2\text{P}}^k$) are shown, along with the squared enhancements, considering the two ring modes as well as the CO stretch mode.

Normal mode	d_k	S_k^{HR}	$\mathcal{E}_{2\text{P}}^{\text{FC},k}$	$ \mathcal{E}_{2\text{P}}^{\text{FC},k} ^2$	$\mathcal{E}_{2\text{P}}^{\text{HT},k}$	$ \mathcal{E}_{2\text{P}}^{\text{HT},k} ^2$	$\mathcal{E}_{2\text{P}}^k$	$ \mathcal{E}_{2\text{P}}^k ^2$
RM1	-0.431	0.093	-0.305	0.093	-1.419	2.013	-0.276	0.076
RM2	0.157	0.012	0.111	0.012	-0.327	0.107	0.123	0.015
CO	0.072	0.003	0.051	0.003	0.166	0.028	0.048	0.002

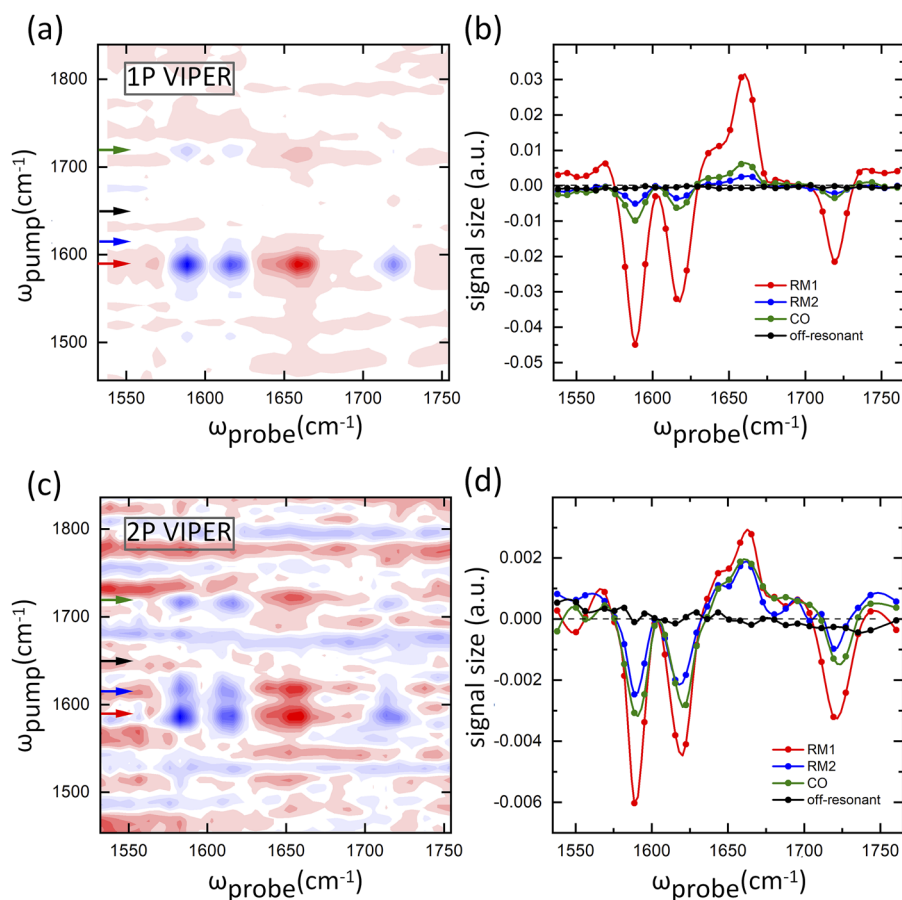


FIG. 3. Experimental one-photon and two-photon VIPER spectra for Coumarin 6. The delay between the last IR pump pulse and the VIS or NIR pump pulse was 0.7 ps, the delay between the VIS or NIR pump pulse and the IR probe pulse was 200 ps. (a) Fourier-transformed two-dimensional (FT-2D) 1P-VIPER spectrum, (b) one-dimensional slices parallel to the probe axis at the frequencies pertaining to the RM1, RM2, and CO modes, as well as an off-resonant frequency to judge the data quality, (c) Fourier-transformed two-dimensional (FT-2D) 2P-VIPER spectrum, and (d) one-dimensional slices parallel to the probe axis at the frequencies pertaining to the same modes as above. In the 2D spectra, blue (red) colors denote negative (positive) signal amplitudes. The data points are connected with a spline fit. The positions of the excited IR bands and the off-resonant slice are marked by their respective colors in the 2D spectra.

From panels (b)–(d), we infer that under two-photon excitation, the pre-excitation effect is pronounced for the ring modes RM1 and RM2 [panels (b) and (c)], while it is weak for the CO mode [panel (d)]. This is not dissimilar from the conclusions we drew for the 1P-VIPER spectra. However, RM2 is now predicted to have a slightly stronger enhancement effect than RM1, differently from our earlier one-photon analysis. As for the signature of the CO mode, the enhancement is likely underestimated, as detailed in Sec. IV D.

Furthermore, we illustrate in panel (e) how an immediate, statistical redistribution of the vibrational excess energy by IVR would play out. Based on the result of the Appendix, we identify an effective temperature of $T_{\text{eff}}^{\text{RM2}} = 188.81$ K that results from an excess energy obtained by vibrational pre-excitation of mode RM2. A very similar result is obtained for the other modes, with $T_{\text{eff}}^{\text{RM1}} = 186.44$ K and $T_{\text{eff}}^{\text{CO}} = 193.57$ K, see Sec. S5 of the supplementary material. It is seen that the VIPER effect is lost under these statistical IVR conditions, while the overall heating of the system is reflected in a slight red-shift of the band-edge. One would expect, though, that non-trivial IVR effects could arise if mode-specific vibrational energy transfer sets in and transiently activates modes that did not undergo VIPER excitation in the first place. In the present system, we do not expect any IVR effects between the three VIPER-active modes (RM1, RM2,

and CO), but we would indeed assume that IVR leads to energy redistribution toward a large number of low-frequency modes.

Next, we will unravel the different effects that led to the observed enhancement. To gain insight into the roles of Franck–Condon vs Herzberg–Teller effects, Fig. 5 analyzes the FC vs HT contributions separately. The results can be compared with the enhancements $\mathcal{E}_{2\text{P}}^{\text{FC}}$ and $\mathcal{E}_{2\text{P}}^{\text{HT}}$ introduced in Sec. II C and listed in Table III. A similar analysis was carried out in Ref. 21 for benchmark systems, where 2P spectra also exhibit combinations of FC and HT contributions.

In Figs. 5(a)–5(c), vibronic spectra are shown, where (a) exclusively the FC contribution is accounted for, (b) exclusively the HT terms are computed, and (c) the combined (“total”) spectrum is shown. Considering exclusively the FC contribution leads to a dominance of the RM1 mode [see panel (a)]—exactly as in our previous 1P-VIPER analysis, where only FC contributions were considered (noting that the line shape is independent of the nature of the electronic transition moment). In Fig. 5(b), the HT contribution is shown, which is considerably smaller in amplitude than the FC contribution [the scales of panels (a) vs (b) differ by a factor of 5]. Interestingly, the HT contribution of the RM1 mode to the VIPER effect is strikingly large relative to the pure HT spectral amplitude.

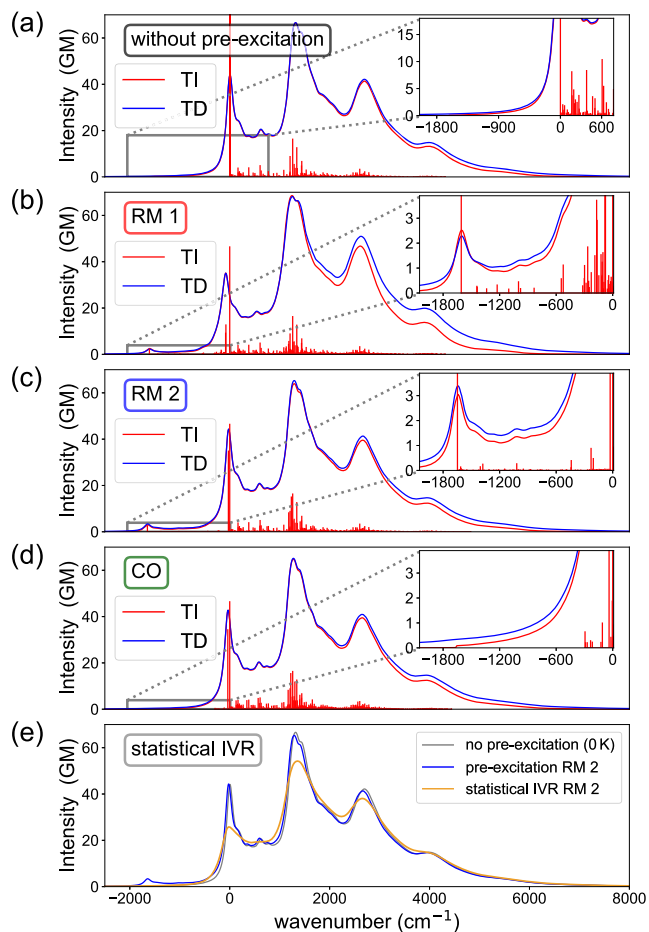


FIG. 4. Computed 2P absorption spectra of Coumarin 6 in THF obtained employing the B3LYP functional and def2-TZVP basis sets, (a) without vibrational pre-excitation, (b) with pre-excitation of the lower-frequency ring mode RM1, (c) with pre-excitation of the higher-frequency ring mode RM2, (d) with pre-excitation of the carbonyl stretch mode CO, and (e) with pre-excitation of the ring mode RM2, such as to compare with a spectrum where the excitation energy is immediately redistributed in a statistical IVR process, here generating an effective temperature of $T_{\text{eff}} = 188.81$ K. Spectra were obtained using either the time-independent approach (red with stick transitions, TI) and convoluted with a Lorentzian envelope function or the time-dependent approach via a Fourier transformation of the analytical correlation functions (blue, TD). The spectrum generated under statistical IVR conditions is shown in orange. Both FC and HT effects were included in the spectra. The origin of the frequency axis is fixed at the 0–0 transition in the absence of vibrational pre-excitation.

This is due to the fact that the 2P transition moment exhibits a pronounced variation with the RM1 mode, much more pronounced than in the case of the RM2 mode or the CO mode (see Sec. S3 of the [supplementary material](#) for the variation of the 2P transition moment as a function of the three relevant modes). This is underscored by [Table III](#), where a large pure-HT enhancement can be inferred for RM1.

Surprisingly, however, the overall (total) spectrum does not show a dominant VIPER effect of the RM1 mode: As already seen in [Fig. 3](#), the RM2 mode gives a slightly larger overall contribution.

This can be explained by the fact that the FC and HT contributions are *not* additive—as can be inferred from the FC/HT cross terms appearing in the expressions of Eqs. (14)–(17) for the spectral intensity. In this particular case, destructive interference takes place, such that the overall (total) spectral intensity is reduced as compared with the individual (hypothetical) FC vs HT intensities.

In [Figs. 5\(d\)–5\(f\)](#), the same data are presented from a different perspective by grouping together the FC, HT, and total spectral intensities for each of the modes and focusing on the low-frequency part of the spectrum, where the VIPER red-shift is observed. As can be seen in [Fig. 4\(d\)](#), the total spectral intensity is significantly reduced as compared with the separate FC vs HT components. Conversely, in the case of the RM2 mode, constructive interference is observed, such that the total spectral intensity is enhanced as compared with the separate spectra. The CO mode shows a very small effect overall. These observations are partially, but not completely captured by the comparison between the predicted partial FC and HT enhancements ($\mathcal{E}_{2P}^{\text{FC}}$ and $\mathcal{E}_{2P}^{\text{HT}}$) and the total enhancements \mathcal{E}_{2P} reported in [Table III](#). This is most likely due to the fact that Duschinsky effects are non-negligible in the Coumarin 6 system.

As a result of the interference effects discussed above, it finally turns out, according to [Figs. 5\(c\)–5\(e\)](#), that the theoretically predicted 2P-VIPER enhancement is slightly larger for the RM2 mode than for the RM1 mode, contrary to expectations from the individual (but hypothetical) FC vs HT spectra. (This effect is not captured by the approximate enhancements \mathcal{E}_{2P} of [Table III](#), even though the trends are correct.) It is clear that the final intensity ratios are the result of a subtle balance between various contributions, which are subject to inaccuracies due to the choice of DFT functionals and the various approximations made in our treatment. As a result, the computational prediction of 2P-VIPER effects is clearly more challenging than the prediction of 1P-VIPER effects, as previously demonstrated for the Coumarin 6 system,⁹ where Herzberg–Teller effects were found to be negligible (see Sec. S4 of the [supplementary material](#)).

D. Comparison with experiment

In [Fig. 6](#), we show a comparison between our theoretical analysis, as discussed above, and the VIPER experiment carried out for the Coumarin 6 system, as reported in [Fig. 3](#). On the l.h.s. of the figure, the experimental results of [Figs. 3\(b\) and 3\(d\)](#) are reproduced. In the upper left panel of [Fig. 6\(a\)](#), the FTIR absorption spectrum in THF is shown, illustrating the relevant vibrational modes; in the upper right panel of [Fig. 6\(d\)](#), the theoretical results are juxtaposed. In [Fig. 6\(b\)](#), experimental 1P-VIPER spectra with pre-excitation of the three relevant modes are shown. Measured data points are connected by a spline fit. Next, [Fig. 6\(c\)](#) shows the 2P-VIPER spectra by comparison. Apart from the much lower intensity—reduced by a factor of ~ 10 —the 2P-VIPER spectra also show a dominant VIPER effect in the RM1 mode but increased activity in the RM2 and CO modes as compared to their 1P-VIPER counterparts. The difference in intensity ratios between 1P-VIPER and 2P-VIPER clearly indicates that a pure FC-based analysis does not hold.

On the r.h.s. of [Fig. 6](#), the theoretical results are juxtaposed. First, the computed IR spectrum, shown in [Fig. 6\(d\)](#), exhibits a typical frequency shift as compared to the experimental data

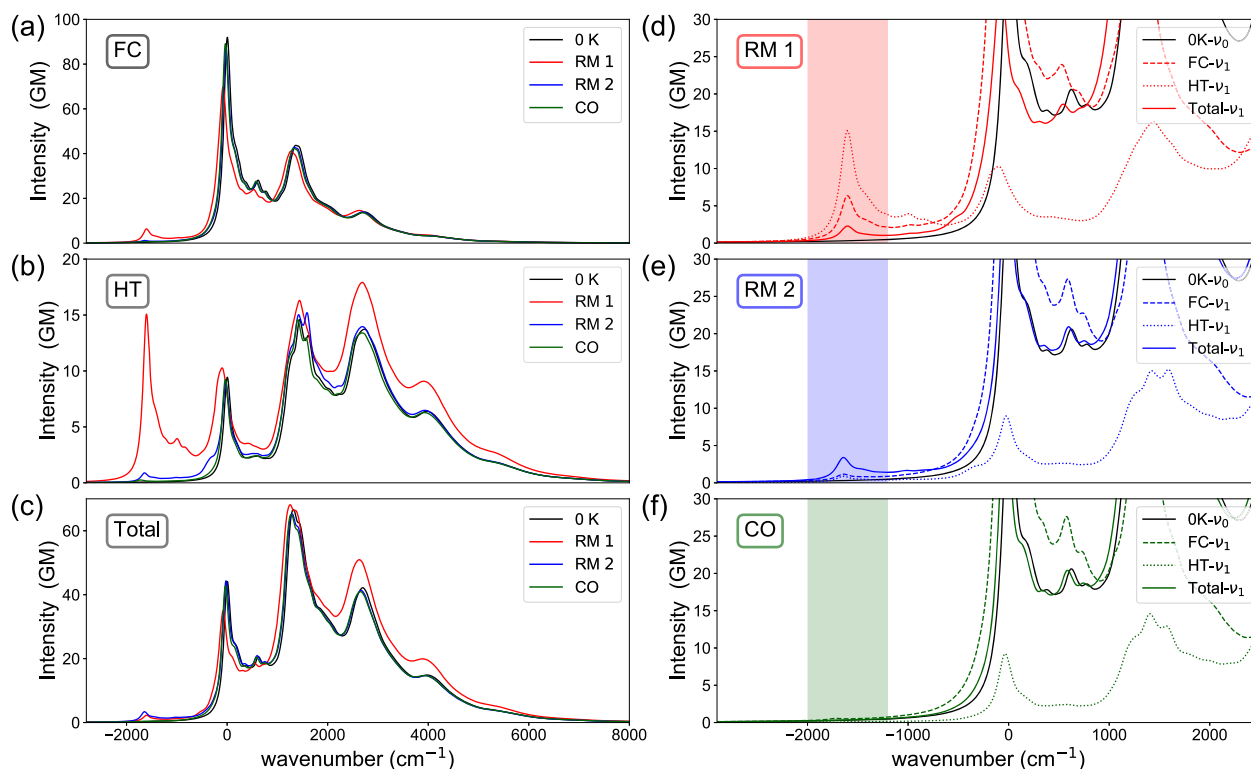


FIG. 5. Computed 2P absorption spectra of Coumarin 6 in THF obtained employing the B3LYP functional and def2-TZVP basis set using the analytical time-dependent approach. The origin of the frequency axis is fixed at the 0–0 transition in the absence of vibrational pre-excitation. Spectra are shown for (a) the pure FC contribution, which is coordinate-independent, (b) the pure HT contribution, which depends on the respective transition moment derivatives, and (c) the complete (“total”) spectra, including the FC and HT contributions and mixed FC-HT terms. Spectra are shown without vibrational pre-excitation (black, $T = 0$ K), with pre-excitation of the lower-frequency ring mode (red, RM1), the higher-frequency ring mode (blue, RM2), and the CO stretch mode (green, CO), respectively. The spectra on the right hand side show a direct comparison of all mentioned contributions, considering (d) pre-excitation of RM1, (e) pre-excitation of RM2, and (f) pre-excitation of the CO stretch mode. The comparison of the pure FC vs HT contributions with the total spectra emphasizes the important role of FC-HT mixed terms and their constructive or destructive influence on 2P absorption.

[the computed frequencies are as follows: 1607.46 cm^{-1} (RM1), 1647.86 cm^{-1} (RM2), and 1730.52 cm^{-1} (CO)], see Table II. Next, the theoretical VIPER spectra are shown [in panels (e) and (f)] for the 1P-VIPER and 2P-VIPER cases, reproduced from the previous figures. As in Ref. 9, we do not directly simulate the experimental spectra but rather infer the relevant VIPER signal size from the vibronic spectra, including pre-excitation. The computed 1P-VIPER spectra, similar (but not identical) to those reported in Ref. 9, reflect a strong enhancement of the 1P cross section after excitation of the RM1 mode, in line with experiment. Moreover, the enhancement ratio between the RM1 vs RM2 modes is similar to experiment. In the 2P-VIPER computation, the presence of FC/HT interference effects leads to a slightly stronger enhancement for the RM2 mode as compared to the RM1 mode, differently from experiment. However, in contrast to the 1P-VIPER analysis, these two modes exhibit similar amplitudes, which does relate to the experimental observations. Hence, our simulations are able to properly describe some qualitative trends observed when going from 1P- to 2P-VIPER—namely, the fact that the relative amplitudes of the two ring modes become closer in the 2P experiment, even though the observed relative

amplitudes (i.e., a larger signal pertaining to RM1 than RM2) are not correctly reproduced in the simulation. The comparison with the CO mode is not consistent, though, since the contribution by the latter is negligible in the computation, whereas this is not the case in the experiment.

When analyzing the cause of the discrepancy between the theoretical predictions and experimental data, the main conclusion is that the interplay between FC and HT effects according to Eqs. (14)–(17) is highly complex and susceptible to shifts due to uncertainties caused by DFT-based approaches. Density functional approximations are known to be of limited reliability in the prediction of two-photon properties^{53–55} and spectral features related to the Herzberg–Teller effect,⁵⁶ and errors incurred at this level are amplified by the complexity of the spectroscopic signatures that are probed in the 2P-VIPER experiment. Furthermore, the situation is exacerbated by solvent effects.⁵⁷ As a result, both the computation of two-photon properties as such and the additional challenge of FC/HT interference effects make the calculations far more challenging than the 1P-VIPER effect that we previously investigated.⁹

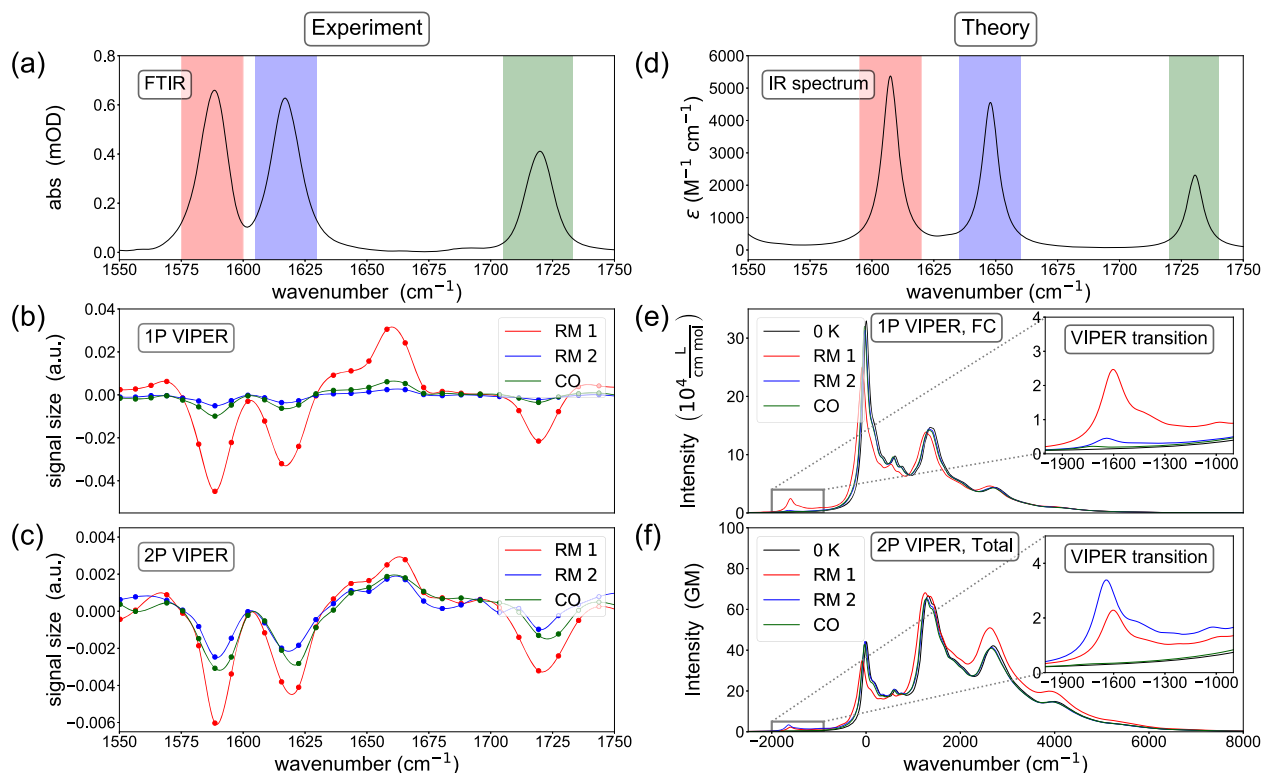


FIG. 6. Comparison of experimental vs theoretical results for 1P-VIPER and 2P-VIPER spectroscopy of the S_1 state of Coumarin 6 in THF; experimental results are shown on the l.h.s., while computational results are shown on the r.h.s., based on the B3LYP functional and def2-TZVP basis set. (a) Experimental Fourier-transform IR (FTIR) spectrum in the region of interest, including two ring modes and the carbonyl stretch mode. (b) Experimental 1P-VIPER spectra after pre-excitation of the lower-frequency ring mode (red, RM1), the higher-frequency ring mode (blue, RM2), and the carbonyl stretch mode (green, CO), recorded using a concentration of 30 mM and an optical path length of 150 μm , see Figs. 3(a) and 3(b) and Secs. III B and IV B for details. (c) Experimental 2P-VIPER spectra after pre-excitation of the relevant modes, see Figs. 3(c) and 3(d) and Secs. III B and IV B for details. (d) Computed infrared spectrum, where the relevant IR transitions show a slight hypsochromic shift, see Table II. (e) Computed 1P vibronic absorption spectra with pre-excitation of the relevant modes, using the TD approach; the color-coding is adapted to the experimental results on the l.h.s. (black: without vibrational pre-excitation, $T = 0$ K, red: pre-excitation of RM1, blue: pre-excitation of RM2, green: pre-excitation of CO); the origin of the frequency axis is fixed at the 0–0 transition in the absence of vibrational pre-excitation. (f) Likewise, the computed 2P vibronic absorption spectra with pre-excitation of the relevant modes are shown, again using the TD approach. For the 1P absorption spectra (e), only the FC contribution was considered, while the 2P spectra (f) take FC as well as HT contributions and mixed FC-HT terms into account. See Sec. IV D for a detailed discussion.

To illustrate this point, Sec. S6 of the [supplementary material](#) shows a comparison with results obtained with the CAM-B3LYP functional, which significantly changes the 2P-VIPER effect prediction for the two ring modes. Using CAM-B3LYP, it turns out that the relative amplitudes of the ring modes are inverted as compared to B3LYP and now correspond to the same sequence as in experiment—but a large intensity difference is observed, which is not in line with experiment.

Other factors arise, related to IVR effects as mentioned above, geometry changes before and after two-photon excitation due to finite pulse durations, deviations from the harmonic model Hamiltonians underlying our analysis, and solvation effects. Several of these aspects are addressed in the [supplementary material](#). Notably, Sec. S3 addresses the role of geometry dependence, and Sec. S7 analyzes an improved treatment of excited-state solvent effects. In the context of the CO mode excitation, we show that the spectral signature is sensitive to the CO bond elongation induced by the electronic

transition, which tends to be underestimated by TDDFT (see Sec. S8) and also depends on the solvent. An increase in bond length consistent with values typically obtained with CASPT2 optimizations⁵⁸ generates a visible VIPER signal for the CO mode. Furthermore, in the gas phase (Fig. S7), the relative intensity of the CO signal is found to be larger than in solution for B3LYP. Regarding the treatment of the solvent, we show in Sec. S7 that a solvent treatment beyond ground-state equilibrium solvation, using the corrected linear response scheme,⁵⁹ leads to an increase in the VIPER effect for all modes, including the CO mode. All of these factors could contribute to capturing the elusive VIPER signal of the CO mode.

Overall, we conclude that the present results are subject to various uncertainties, which explain why the agreement with experiment is less good than expected from our previous 1P-VIPER study (noting, though, that the latter did not achieve quantitative agreement with experiment). Even so, the results we present here appear reasonable, even though they are not quantitative.

V. DISCUSSION AND CONCLUSIONS

In this joint experimental and theoretical work, a proof of principle is given of the experimental feasibility of the two-photon VIPER experiment and its theoretical analysis. Connecting to our earlier work on one-photon VIPER, we addressed the Coumarin 6 chromophore, focusing on the same electronic $S_1 \leftarrow S_0$ transition that was investigated in our earlier work. This allows us to carry out a meaningful comparison between 1P-VIPER and 2P-VIPER results, showing that a reasonable—even though not quantitative—interpretation can be given by theoretical/computational analysis.

The 2P-VIPER set-up proves challenging both on the experimental and theoretical sides, due to the small intensities as compared to the one-photon case. In the case of Coumarin 6, the chosen target state (S_1) indeed exhibits moderate to small two-photon activity, as compared with a higher-lying state (S_3), which exhibits a much larger two-photon cross section. Future work is planned to address electronic states with marked two-photon activity in other relevant systems.

On the theory side, the analysis necessitates the inclusion of Herzberg–Teller effects, which were disregarded in our earlier 1P-VIPER study due to their negligible contribution to the one-photon process. This complicates the picture and leads to the appearance of non-trivial interference effects between the Franck–Condon (FC) and Herzberg–Teller (HT) contributions. We analyzed in some detail how these interference effects affect the VIPER enhancement, showing that HT effects significantly change the relative VIPER signals between different modes, in qualitative agreement with the experimental observations. The theoretical framework developed here is of general relevance for the description of such FC/HT interference effects and their complex—and sometimes nonintuitive—spectroscopic manifestations. These considerations will play out in other types of electronic-vibrational spectroscopies, beyond 2P-VIPER.

The computational procedure, based on density functional approximations, proves challenging due to the subtle interplay between effects that are strongly susceptible to inaccuracies in the DFT functionals. Due to the size of the Coumarin 6 molecule, high-level electronic structure methods, notably coupled-cluster approaches, which are far more reliable in the 2P spectroscopy context,⁶⁰ are out of reach. Comparisons between selected DFT functionals in our study, notably the B3LYP hybrid functional and the CAM-B3LYP range-separated hybrid functional, show that the spectroscopic signatures differ significantly. These conclusions are in line with the current literature, which gives a critical assessment of DFT functionals in the context of 2P properties,^{53–55} putting the widespread use of density functional approximations in this area in perspective.

Furthermore, the present analysis was restricted to a harmonic approximation (including Duschinsky rotation effects). While this should be a reasonable approximation for the high-frequency VIPER-active modes under study, this limitation can be removed in future work by including anharmonicities and using more flexible numerical time-dependent methodologies as exemplified in Ref. 9. In addition, simulations comprising IVR mechanisms may help to improve the match between the theoretical and experimental results. Finally, higher excited states with non-negligible two-photon

activity could interfere with the 2PA cross section, and two-step channels could play a role.^{61,62}

Overall, the present protocol does not yet use the most general simulation framework but offers the first applications of a predictive tool for the identification of optimal VIPER-active modes under two-photon excitation.

SUPPLEMENTARY MATERIAL

See the [supplementary material](#) (part I) for a characterization of the low-lying singlet states of Coumarin 6 (Sec. S1), a comparison of DFT functionals and basis sets (Sec. S2), details on the geometry dependence of two-photon transition moment tensor (Sec. S3), an analysis of Herzberg–Teller effects in 1P-VIPER spectroscopy (Sec. S4), additional material on statistical IVR and temperature effects (Sec. S5), an assessment of the effect of different DFT functionals on 2P-VIPER spectra (Sec. S6), the description of solvent effects using the corrected linear response method (Sec. S7), and an analysis of the CO bond length on the 2P-VIPER signature (Sec. S8). Additionally, a second part of the [supplementary material](#) (part II) provides detailed formal derivations of the 2P-VIPER expressions as implemented in the *FCclasses3* code.

ACKNOWLEDGMENTS

Funding by the Deutsche Forschungsgemeinschaft (DFG) via the CLiC graduate school (Grant No. RTG 1986, Complex Light-Control) is gratefully acknowledged. L.J.G.W.V.W. thanks the DFG for funding (Grant No. 466145756). J.C. thanks the Ministerio de Universidades, Plan de Recuperación, Transformación y Resiliencia, and UAM for funding the research stay in Pisa with a requalification program (Grant No. CA2/RSUE/2021-00890). F.S. acknowledges financial support from ICSC – Centro Nazionale di Ricerca in High Performance Computing, Big Data and Quantum Computing, funded by European Union – NextGenerationEU - PNRR, Missione 4 Componente 2 Investimento 1.4.

AUTHOR DECLARATIONS

Conflict of Interest

The authors have no conflicts to disclose.

Author Contributions

M.H., H.M.A.M., H.B., and J.C. contributed equally to this work.

Maximiliane Horz: Formal analysis (lead); Investigation (lead); Methodology (supporting); Validation (equal); Visualization (lead); Writing – original draft (supporting); Writing – review & editing (equal). **Hafiz M. A. Masood:** Formal analysis (lead); Investigation (lead); Methodology (supporting); Validation (equal); Visualization (supporting); Writing – original draft (supporting); Writing – review & editing (equal). **Hendrik Brunst:** Formal analysis (lead); Investigation (lead); Methodology (lead); Validation (equal); Visualization (supporting); Writing – original draft (supporting); Writing – review & editing (equal). **Javier Cerezo:** Formal analysis (lead); Funding acquisition (supporting); Methodology (lead); Writing – review & editing (equal). **David Picconi:** Formal analysis

(supporting); Methodology (supporting); Validation (supporting). **Hannah Vormann**: Formal analysis (supporting); Investigation (supporting); Validation (supporting). **Madhava Shyam Niraghatam**: Investigation (supporting). **Luuk J. G. W. van Wilderen**: Conceptualization (equal); Funding acquisition (supporting); Methodology (lead); Supervision (equal); Writing – review & editing (equal). **Jens Bredenbeck**: Conceptualization (equal); Funding acquisition (lead); Methodology (lead); Project administration (equal); Resources (equal); Supervision (equal); Writing – review & editing (equal). **Fabrizio Santoro**: Conceptualization (equal); Formal analysis (lead); Methodology (lead); Resources (equal); Writing – review & editing (equal). **Irene Burghardt**: Conceptualization (equal); Formal analysis (lead); Funding acquisition (lead); Methodology (lead); Project administration (equal); Resources (equal); Supervision (equal); Writing – original draft (lead); Writing – review & editing (equal).

DATA AVAILABILITY

The original experimental data that support the findings of this study are available from the corresponding authors upon reasonable request. The theoretical data that support the findings of this study are available within the article and its [supplementary material](#).

APPENDIX: COMPUTATION OF EFFECTIVE VIPER TEMPERATURE UNDER QUASI-EQUILIBRATION CONDITIONS

Relating to the discussion of Sec. IV C and the simulations of Fig. 4(e), we explain here how the effective temperature of the molecular system can be estimated under the assumption that the VIPER excess energy is immediately thermalized. To this end, we use the fact that the internal energy U for N oscillators at temperature T is given by the Bose–Einstein distribution,

$$U = \sum_{n=1}^N \hbar\omega_n \left(\frac{1}{e^{\beta\hbar\omega_n} - 1} + \frac{1}{2} \right) = \sum_{n=1}^N \frac{\hbar\omega_n}{2} \coth\left(\frac{\beta\hbar\omega_n}{2}\right), \quad (\text{A1})$$

where $\beta = 1/(k_B T_0)$ refers to the reference temperature T_0 , e.g., room temperature.

Now, we compute the effective temperature T_{eff} , which would correspond to the situation where the excess energy ΔE from the VIPER experiment—i.e., the extra vibrational quantum that is placed into the VIPER active mode—is instantaneously distributed over all oscillators. To this end, we define $\beta_{\text{eff}} = 1/(k_B T_{\text{eff}})$, where T_{eff} is the effective temperature, and we introduce the modified internal energy U' such that

$$U' - U = \Delta E, \quad (\text{A2})$$

or

$$\sum_{n=1}^N \hbar\omega_n \left(\frac{1}{e^{\beta_{\text{eff}}\hbar\omega_n} - 1} - \frac{1}{e^{\beta\hbar\omega_n} - 1} \right) = \Delta E, \quad (\text{A3})$$

where the zero-point energy is seen to drop out of the difference. By inverting the above relation, we obtain $\beta_{\text{eff}}(\Delta E)$ or $T_{\text{eff}}(\Delta E)$; in practice, this is done numerically.

REFERENCES

- J. N. Mastron and A. Tokmakoff, *J. Phys. Chem. A* **120**, 9178 (2016).
- T. L. Courtney, Z. W. Fox, K. M. Slenkamp, and M. Khalil, *J. Chem. Phys.* **143**, 154201 (2015).
- T. L. Courtney, Z. W. Fox, L. Estergreen, and M. Khalil, *J. Phys. Chem. Lett.* **6**, 1286 (2015).
- L. J. G. W. van Wilderen and J. Bredenbeck, *Angew. Chem., Int. Ed.* **54**, 11624 (2015).
- L. J. G. W. van Wilderen, A. T. Messmer, and J. Bredenbeck, *Angew. Chem., Int. Ed.* **53**, 2667 (2014).
- D. Kern-Michler, C. Neumann, N. Mielke, L. J. G. W. van Wilderen, M. Reinfelds, J. von Cosel, F. Santoro, A. Heckel, I. Burghardt, and J. Bredenbeck, *J. Am. Chem. Soc.* **140**, 926 (2018).
- H. Brunst, H. M. A. Masood, A. R. Thun, A. Kondratiev, G. Wille, L. J. G. W. van Wilderen, and J. Bredenbeck, *Angew. Chem., Int. Ed.* **61**, e202211490 (2022).
- P. Klán, T. Šolomek, C. G. Bochet, A. Blanc, R. Givens, M. Rubina, V. Popik, A. Kostikov, and J. Wirz, *Chem. Rev.* **113**, 119 (2013).
- J. von Cosel, J. Cerezo, D. Kern-Michler, C. Neumann, L. J. G. W. van Wilderen, J. Bredenbeck, F. Santoro, and I. Burghardt, *J. Chem. Phys.* **147**, 164116 (2017).
- M. Göppert-Mayer, *Ann. Phys.* **401**, 273 (1931).
- W. M. McClain, *Acc. Chem. Res.* **7**, 129 (1974).
- J. D. Bhawalkar, G. S. He, and P. N. Prasad, *Rep. Prog. Phys.* **59**, 1041 (1996).
- G. Herzberg and E. Teller, *Z. Phys. Chem.* **21B**, 410–446 (1933).
- G. J. Small, *J. Chem. Phys.* **54**, 3300 (1971).
- F. Duschinsky, *Acta Physicochim. USSR* **7**, 551 (1937).
- N. J. Turro, *Modern Molecular Photochemistry* (Cummings Publishing Company, 1978).
- F. Santoro, R. Improta, A. Lami, J. Bloino, and V. Barone, *J. Chem. Phys.* **126**, 084509 (2007).
- F. Santoro and J. Cerezo, *FCclasses3*, a code for vibronic calculations, visit: <http://www.iccom.cnr.it/en/fcclasses>, 2022.
- J. Cerezo and F. Santoro, *J. Comput. Chem.* **44**, 626 (2023).
- F. Santoro, A. Lami, R. Improta, and V. Barone, *J. Chem. Phys.* **126**, 184102 (2007).
- P. Macak, Y. Luo, and H. Ågren, *Chem. Phys. Lett.* **330**, 447 (2000).
- P. Norman, Y. Luo, and H. Ågren, *J. Chem. Phys.* **111**, 7758 (1999).
- P. R. Monson and W. M. McClain, *J. Chem. Phys.* **53**, 29 (1970).
- Y. R. Shen, *The Principles of Nonlinear Optics* (Wiley, New York, 1984).
- K. Aidas, C. Angeli, K. L. Bak, V. Bakken, R. Bast, L. Boman, O. Christiansen, R. Cimraglia, S. Coriani, P. Dahle, E. K. Dalskov, U. Ekström, T. Enevoldsen, J. J. Eriksen, P. Ettenhuber, B. Fernández, L. Ferrighi, H. Fliegl, L. Frediani, K. Hald, A. Halkier, C. Hättig, H. Heiberg, T. Helgaker, A. C. Hennum, H. Hettema, E. Hjertenaes, S. Høst, I.-M. Høyvik, M. F. Iozzi, B. Jansík, H. J. A. Jensen, D. Jonsson, P. Jørgensen, J. Kauczor, S. Kirpekar, T. Kjaergaard, W. Klopper, S. Knecht, R. Kobayashi, H. Koch, J. Kongsted, A. Krapp, K. Kristensen, A. Ligabue, O. B. Lutnaes, J. I. Melo, K. V. Mikkelsen, R. H. Myhre, C. Neiss, C. B. Nielsen, P. Norman, J. Olsen, J. M. H. Olsen, A. Osted, M. J. Packer, F. Pawłowski, T. B. Pedersen, P. F. Provasi, S. Reine, Z. Rinkevicius, T. A. Ruden, K. Ruud, V. V. Rybkin, P. Salek, C. C. M. Samson, A. S. de Merás, T. Saue, S. P. A. Sauer, B. Schimmelpfennig, K. Sneskov, A. H. Steindal, K. O. Sylvester-Hvid, P. R. Taylor, A. M. Teale, E. I. Tellgren, D. P. Tew, A. J. Thorvaldsen, L. Thøgersen, O. Vahtras, M. A. Watson, D. J. D. Wilson, M. Ziolkowski, and H. Ågren, “The Dalton quantum chemistry program system,” *Wiley Interdiscip. Rev.: Comput. Mol. Sci.* **4**, 269 (2014).
- F. Santoro and A. Lami, “Time-dependent approaches to calculation of steady-state vibronic spectra: From fully quantum to classical approaches,” in *Computational Strategies for Spectroscopy: From Small Molecules to Nano Systems*, edited by V. Barone (John Wiley & Sons, Inc., 2012), Chap. 10, pp. 475–516.
- D. J. Tannor, *Introduction to Quantum Mechanics: A Time-Dependent Perspective*, 1st ed. (University Science Books, 2007).
- F. J. Avila Ferrer, J. Cerezo, J. Soto, R. Improta, and F. Santoro, *Comput. Theor. Chem.* **1040-1041**, 328 (2014).
- A. Baiardi, J. Bloino, and V. Barone, *J. Chem. Theory Comput.* **9**, 4097 (2013).
- R. Ianculescu and E. Pollak, *J. Phys. Chem. A* **108**, 7778 (2004).

- ³¹J. Tatchen and E. Pollak, *J. Chem. Phys.* **128**, 164303 (2008).
- ³²J. Tang, M. T. Lee, and S. H. Lin, *J. Chem. Phys.* **119**, 7188 (2003).
- ³³Y. J. Yan and S. Mukamel, *J. Chem. Phys.* **85**, 5908 (1986).
- ³⁴S. Mukamel, S. Abe, and R. Islampour, *J. Phys. Chem.* **89**, 201 (1985).
- ³⁵R. Kubo and Y. Toyozawa, *Prog. Theor. Phys.* **13**, 160 (1955).
- ³⁶J. Huh and R. Berger, *J. Phys.: Conf. Ser.* **380**, 012019 (2012).
- ³⁷A. Baiardi, J. Bloino, and V. Barone, *J. Chem. Phys.* **141**, 114108 (2014).
- ³⁸Q. Peng, Y. Niu, C. Deng, and Z. Shuai, *Chem. Phys.* **370**, 215 (2010).
- ³⁹S. Mukamel, *Principles of Nonlinear Optical Spectroscopy*, 1st ed. (Oxford University Press, Oxford, 1999).
- ⁴⁰J. Bredenbeck and P. Hamm, *Rev. Sci. Instrum.* **74**, 3188 (2003).
- ⁴¹P. Hamm, R. A. Kaindl, and J. Stenger, *Opt. Lett.* **25**, 1798 (2000).
- ⁴²J. Helbing and P. Hamm, *J. Opt. Soc. Am. B* **28**, 171 (2011).
- ⁴³E. Deniz, K. B. Eberl, and J. Bredenbeck, *Rev. Sci. Instrum.* **89**, 116101 (2018).
- ⁴⁴M. J. Frisch, G. W. Trucks, H. B. Schlegel, G. E. Scuseria, M. A. Robb, J. R. Cheeseman, G. Scalmani, V. Barone, G. A. Petersson, H. Nakatsuji, X. Li, M. Caricato, A. V. Marenich, J. Bloino, B. G. Janesko, R. Gomperts, B. Mennucci, H. P. Hratchian, J. V. Ortiz, A. F. Izmaylov, J. L. Sonnenberg, D. Williams-Young, F. Ding, F. Lipparini, F. Egidi, J. Goings, B. Peng, A. Petrone, T. Henderson, D. Ranasinghe, V. G. Zakrzewski, J. Gao, N. Rega, G. Zheng, W. Liang, M. Hada, M. Ehara, K. Toyota, R. Fukuda, J. Hasegawa, M. Ishida, T. Nakajima, Y. Honda, O. Kitao, H. Nakai, T. Vreven, K. Throssell, J. A. Montgomery, Jr., J. E. Peralta, F. Ogliaro, M. J. Bearpark, J. J. Heyd, E. N. Brothers, K. N. Kudin, V. N. Staroverov, T. A. Keith, R. Kobayashi, J. Normand, K. Raghavachari, A. P. Rendell, J. C. Burant, S. S. Iyengar, J. Tomasi, M. Cossi, J. M. Millam, M. Klene, C. Adamo, R. Cammi, J. W. Ochterski, R. L. Martin, K. Morokuma, O. Farkas, J. B. Foresman, and D. J. Fox, Gaussian 16 Revision B.01, Gaussian, Inc., Wallingford, CT, 2016.
- ⁴⁵A. D. Becke, *J. Chem. Phys.* **98**, 5648 (1993).
- ⁴⁶A. D. Becke, *J. Chem. Phys.* **98**, 1372 (1993).
- ⁴⁷F. Weigend and R. Ahlrichs, *Phys. Chem. Chem. Phys.* **7**, 3297 (2005).
- ⁴⁸F. Weigend, *Phys. Chem. Chem. Phys.* **8**, 1057 (2006).
- ⁴⁹T. Yanai, D. P. Tew, and N. C. Handy, *Chem. Phys. Lett.* **393**, 51 (2004).
- ⁵⁰J.-D. Chai and M. Head-Gordon, *Phys. Chem. Chem. Phys.* **10**, 6615 (2008).
- ⁵¹S. Miertuš, E. Scrocco, and J. Tomasi, *Chem. Phys.* **55**, 117 (1981).
- ⁵²S. Miertuš and J. Tomasi, *Chem. Phys.* **65**, 239 (1982).
- ⁵³M. Chołuj, M. M. Alam, M. T. P. Beerepoot, S. P. Sitkiewicz, E. Matito, K. Ruud, and R. Zalesny, *J. Chem. Theory Comput.* **18**, 1046 (2022).
- ⁵⁴M. T. P. Beerepoot, D. H. Friese, N. H. List, J. Kongsted, and K. Ruud, *Phys. Chem. Chem. Phys.* **17**, 19306 (2015).
- ⁵⁵E. Rudberg, P. Salek, T. Helgaker, and H. Ågren, *J. Chem. Phys.* **123**, 184108 (2005).
- ⁵⁶A. Manian, R. A. Shaw, I. Lyskov, W. Wong, and S. P. Russo, *J. Chem. Phys.* **155**, 054108 (2021).
- ⁵⁷R. Di Remigio, T. Giovannini, M. Ambrosetti, C. Cappelli, and L. Frediani, *J. Chem. Theory Comput.* **15**, 4056 (2019).
- ⁵⁸C. A. Guido, D. Jacquemin, C. Adamo, and B. Mennucci, *J. Phys. Chem. A* **114**, 13402 (2010).
- ⁵⁹M. Caricato, B. Mennucci, J. Tomasi, F. Ingrosso, R. Cammi, S. Corni, and G. Scalmani, *J. Chem. Phys.* **124**, 124520 (2006).
- ⁶⁰C. Hättig, O. Christiansen, and P. Jørgensen, *J. Chem. Phys.* **108**, 8331 (1998).
- ⁶¹A. Baev, F. Gel'mukhanov, P. Macák, Y. Luo, and H. Ågren, *J. Chem. Phys.* **117**, 6214 (2002).
- ⁶²S. Polyutov, I. Minkov, F. Gel'mukhano, and H. Ågren, *J. Phys. Chem. A* **109**, 9507 (2005).